TECHNISCHE UNIVERSITÄT WIEN
Vienna University of Technology

DIPLOMARBEIT

A Feasibility Study of a Bone-Screw microFE Model

ausgeführt zum Zwecke der Erlangung
des akademischen Grades eines Diplom-Ingenieurs
unter Leitung von

Privat-Doz. Dipl.-Ing. Dr. techn. Dieter H. Pahr

Institut für Leichtbau und Struktur-Biomechanik (E317)

eingereicht an der Technischen Universität Wien
Fakultät für Maschinenwesen und Betriebswissenschaften

von

Lukas Peyker
E700/9925420
Raffaelg. 32/8
1200 Wien

Wien, im Januar 2012 Lukas Peyker

Acknowledgements

The planning, organization and execution of this thesis would not have been possible without the gracious support of several people.

First, I want to thank my advisor Dr. Dieter Pahr who had the initial idea for this thesis and provided the necessary support at all steps of the process. He was always around to answer questions or provided practical help.

The setup as well as the execution of the mechanical test would not have been possible without the generous help of Enrico Dall'Ara. His experience in biomechanical testing ensured the successful generation of the mechanical test data.

I am very grateful to Prof. Michael Pretterklieber from the Center for Anatomy and Cell Biology at the AKH Wien, who provided the radius bones that were used in the mechanical tests.

For providing the locking screws and performing their implantation into the radius bones I have to thank Dr. Patrick Weninger from the Lorenz Böhler Unfall-Krankenhaus Wien. Additionally, he provided valuable insight into the clinical background and the application of the volar plate osteosynthesis.

During the preliminary test run which preceded the definition of the final test design, Dr. Peter Varga was of great help to me. I also want to thank him for establishing the contact to Lukas Fischer and René Donner from the Institute for Computational Image Analysis and Radiology at the AKH Wien. They were kind enough to provide the central algorithm used for the metal artifact reduction.

For his support during the CT scanning process I am grateful to Thomas Gross.

I want to thank my colleague Alfonso Bartolomé who worked on his own thesis at the ILSB and with whom I spend a lot of time in the FE lab sharing the minor grievances and small triumphs that working on a master thesis provides.

Finally, I want to thank my parents who have been and continue to be a constant source of support and encouragement.

Abstract

The finite element method is increasingly employed in biomechanical investigations. This thesis takes the example of the volar plate osteosynthesis of the human radius as a starting point for a comparison between a FE analysis and a mechanical test. A simple model of a titanium screw which was implanted in a cropped bone sample and subjected to a defined displacement was derived. Five different FE configurations were created from CT data and compared to test results. These FE models were used to study the influence of the contact between bone and screw as well as the feasibility of a virtually inserted screw. The effect of the implantation process on the FE model generation was also discussed. Furthermore, the influence of the resolution of the CT data on the FE results was studied.

This thesis shows that linear microFE modelling of the screw/bone interface leads to an over-estimation of the spring stiffness of the connection in comparison to the data from the mechanical test. Different modelling strategies were used to investigate this effect. One model with perfect bonding between bone and screw gives a stiffness overestimation of 67 %. Another model that takes the contact between bone and screw into account gives a reduction of this over-estimation to 41 %. Additionally, removing those trabeculae from the model that were broken during the implantation process leads to a further decrease in spring stiffness (3 % over-estimation). On the other hand, the model created by virtually inserting the screw gives a spring stiffness that is 89 % higher than the measured value from the mechanical test.

In conclusion, microFE models are well suited for the investigation of bone/screw models, however non-linear considerations will be needed to improve the predictability.

Zusammenfassung

Die Finite Elemente Methode wird mehr und mehr im Zuge biomechanischer Untersuchungen eingesetzt. Die vorliegende Diplomarbeit nimmt das Beispiel der volaren Platten-Osteosynthese am menschlichen Radiusknochen zum Ausgangspunkt für einen Vergleich zwischen einer FE Analyse und einem mechanischen Experiment. Es wurde ein einfaches Modell einer in eine zugeschnittene Knochenprobe implantierten und mit einer definierten Verschiebung beaufschlagten Schraube aufgestellt. Fünf verschiedene FE Konfigurationen basierend auf CT Scans wurden erstellt und den experimentellen Ergebnissen gegenüber gestellt. Die FE Modelle untersuchen den Einfluss, den der Kontakt zwischen Knochen und Schraube hat und die Machbarkeit einer virtuell eingefügten Schraube. Weiters werden die Auswirkungen des Implantationsprozesses auf die FE Modellgenerierung diskutiert. Außerdem wurde der Einfluss, den die Auflösung der CT Daten auf die FE Ergebnisse hat, untersucht.

Diese Diplomarbeit zeigt, dass eine lineare FE Modellierung der Schraube/Knochen-Verbindung zu einer Überschätzung der Federsteifigkeit der Verbindung führt, wenn man die Ergebnisse des mechanischen Tests zum Vergleich heranzieht. Verschiedene Modellierungsstrategien wurden eingesetzt um diesen Effekt zu untersuchen. Ein Modell mit perfekter Bindung zwischen Knochen und Schaube liefert eine Überschätzung der Steifigkeit um 67 %. Ein anderes FE Model, das den Kontakt zwischen Schraube und Knochen berücksichtigt zeigt eine Reduktion der Überschätzung auf 41 %. Werden zusätzlich die bei der Implantation gebrochenen Trabekel aus dem Model entfernt zeigt sich ein weiteres Absinken der Federsteifigkeit (3 % Überschätzung). Das Model mit der virtuell eingefügten Schraube führte andererseits zu einer Steifigkeit, die 89 % höher als der beim mechanischen Test gemessene Wert ist.

Zusammenfassend lässt sich sagen, dass FE Modelle für die Untersuchung von Schraube/Knochen-Modellen gut geeignet sind, aber nichtlineare Betrachtungen benötigt werden um die Vorhersagbarkeit zu erhöhen.

Contents

List of Figures

List of Tables

1. Introduction

This chapter gives an introduction of the topics that are important in the context of this thesis. The morphological and mechanical properties of bone are discussed. Osteoporosis, a prevalent disease that reduces the mechanical properties of bone dramatically, is addressed afterwards. Focusing on the distal radius as a common site of osteoporosis related fractures, an overview of the anatomy and of the characteristics of a fracture of this bone is given. The treatment of bone fractures is outlined with emphasis on the volar plate-osteosynthesis. Because numerical methods are used in this work, the use of the finite element method in biomechanics is addressed. Finally, the aim and scope of this thesis are summarized.

1.1. Bone

Bone is one of the major components of the human body. It is designed to fulfill a variety of physiological functions [1]. Together with muscles and tendons, bones constitute the skeletal system that is necessary for the motor activity and locomotion of the body. The bones of the thorax and head shield the inner organs. Besides these mechanical functions bone has also metabolical functions. The osseous material functions as a reservoir for the body's mineral reserves (especially calcium). The marrow that fills the inside of bones is responsible for the production of blood cells.
Like all biological material bone is organized in a complex hierarchical structure [2, 3] (see Figure 1.1 for an overview and scales). The nano level consists of arrays of bone fibrils. Each

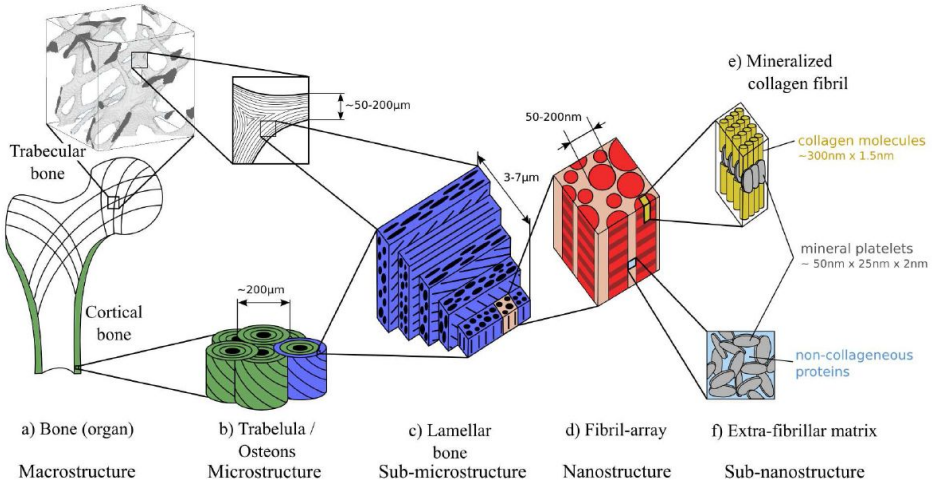

Figure 1.1.: The microstructural organisation of bone (source: [4]).

fibril is a stacked assembly of collagen molecules and mineral crystals (primarily hydroxylapatit). The fibril arrays are organized in layers of unidirectional fibril orientation, the lamellae. These lamellae are the building blocks of two different types of microstructure: *cortical bone* and *trabecular bone*.

Cortical bone is the denser material constituting the shell of bones. It consists of concentrically organized lamellae that form interpenetrating cylindrical structures, called osteons. While each layer consists of unidirectional collagen fibers, neighbouring layers show different fiber orientations. In the hollow center of the osteon lies the Haversian canal that houses the vascular and nervous infrastructure of the bone. The axis of an osteon is generally oriented in parallel to the surface and roughly oriented along the main loading direction in the cortex. Trabecular bone is a sponge-like structure found in the epiphysis of long bones and in the center of vertebrae. Here the lamellae form a network of interconnected plates and rods, called trabeculae, whose main orientation corresponds to the direction of the principal stresses caused by muscular forces and body weight acting on the bone. The volume between the trabeculae is filled with marrow.
The microarchitecture of bone is subjected to a constant remodeling process (Figure 1.2). Two

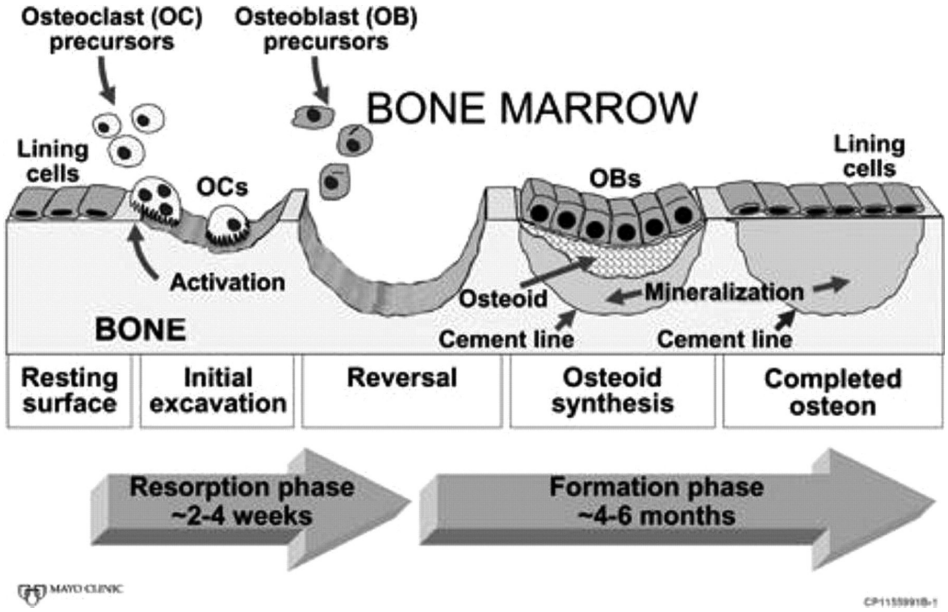

Figure 1.2.: A schematic representation of the remodeling process of bone. The osteoclasts (OCs) remove bone and the osteoblasts (OBs) rebuild it (source: [5]).

types of cells are active in this process. *Osteoclasts* remove small crescent shaped volumes of bone (bone resorption), while *osteoblasts* fill these volumes again with new bone substance (bone formation). This constant remodeling is necessary to enable the repair of damaged bone and to adapt the bone structure to long term changes in the loading conditions. Frost identifies the mechanical peak strain in the bone as the driving factor behind bone remodeling and postulates two strain thresholds [6]. If the local peak strain lies below the lower threshold, bone material is reduced in that region. A local peak strain above the upper threshold leads to a local increase in bone deposition. Between the two thresholds lies the area of healthy bone maintenance, where bone resorption and deposition are in balance and the bone mass stays the same. As the process takes place at the surface of the microstructure, the higher surface to volume ratio leads to a higher remodeling activity in trabecular bone compared to cortical bone [3]. The higher bone turnover is beneficial with respect to the aforementioned adjustment of trabecular orientations to principal stress directions. On the other hand, an imbalance in the remodeling process will manifest itself in a distinctly changed trabecular

structure (see Section 1.2).

The study of the mechanical properties of bone is subject to ongoing research. Experimental studies suggest a difference of 20-30% between cortical and trabecular bone in terms of tissue level elastic modulus [10]. The range of values found for the elastic modulus is relatively wide with reported values between 2 and 20 GPa, whereas reasonable values for wet tissue are found around 8 to 15 GPa [7, 8, 9]. This significant gap could be due to differences in the testing setup and the preparation of the tested material.

1.2. Osteoporosis

Osteoporosis is defined by the World Health Organization as a "disease characterised by low bone mass and microarchitectural deterioration of bone tissue, leading to enhanced bone fragility and a consequent increase in fracture risk"[11]. Symptomatic for the disease is an imbalance in the remodeling process (see Section 1.1). If the activity of osteoclasts exceeds that of the osteoblasts, more bone material is resorbed than gets deposited. This continually reduces the thickness of the cortical shell and of individual trabeculae (Figure 1.3). As a result the affected bone can sustain less stress and the fracture risk grows. The mechanisms that

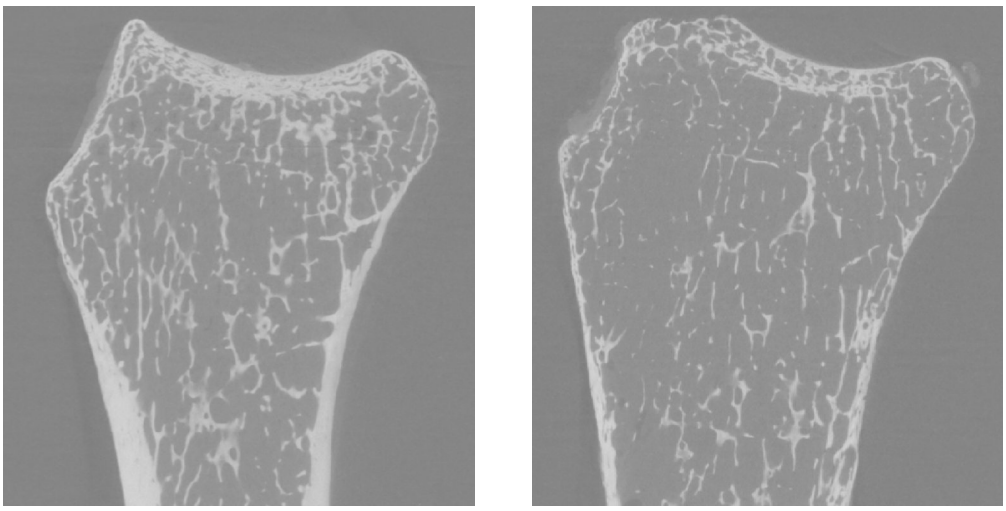

(a) (b)

Figure 1.3.: Sagittal plane from the left distal radius from two women age 48 (a) and age 93 (b) at approximately the same anatomical region. Note the microstructural differences like the thickness and porosity of the cortical shell, the density of the trabecular network and the thickness and connectivity of individual trabeculae.

lead to osteoporosis are highly complex as the formation, activation and resorption of osteoclasts and osteoblasts are governed by a variety of interdependent processes involving multiple components. The metabolisms of estrogen and calcium seem to play an important part as well as genetic factors, but the exact interactions are still part of scientific investigations. For a recent review of the state of knowledge see [12].
The disease can affect both sexes, but the osteoporotic fracture risk for women is significantly higher than for men (about 2-3 times). Reasons for this gender difference are lower peak bone

mass (meaning the maximum of bone mass reached in a persons lifetime), accelerated bone loss following menopause and a higher life expectancy [11].

1.3. Fracture of the Distal Radius

One region of the human body that is often affected by the hightened fracture risk due to osteoporotic bone loss is the distal end of the radius. The radius is a long bone of the upper extremity. Together with the ulna it forms the forearm (Figure 1.4) and enables the supination and pronation of the hand. The proximal end of the radius is part of the elbow joint, the distal end is part of the wrist.

Causes for distal radius fractures can be high energy trauma sustained during car crashes or

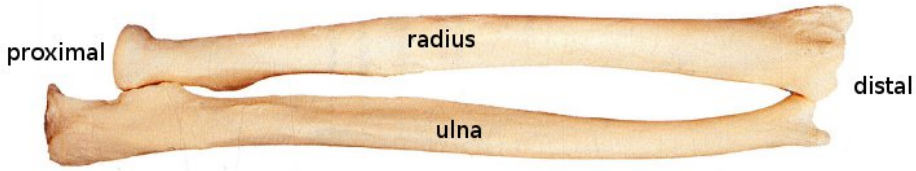

Figure 1.4.: The skeletal anatomy of the human forearm (source: [13]).

low energy trauma from a fall on the outstreched hand. The latter is especially prevalent in older women (see Section 1.2). A 1994 report by the WHO estimates a 15% risk for European women to suffer a wrist fracture in their lifetime and notes that "about 20% of 70-year-old women have had at least one wrist fracture" [11].

The most frequent kind of distal radius fracture among the recorded cases is the *Colles' fracture*, which is associated with a fall on the outstretched hand [14, 15, 16]. It is characterized by a transverse crack about 2-3 cm from the distal end, a dorsal tilt of the fragment and radial shortening (Figure 1.5).

Figure 1.5.: X-ray image of a Colles' fracture. The red ellipse marks the location of the fracture (source: [17]).

1.4. Volar Plate-Osteosynthesis

Roughly speaking, two steps are necessary in the treatment of a broken bone. First, the repositioning of the fractured piece(s) to the anatomically correct place (called *reduction*) and second, stabilization of the fracture site to ensure proper healing (called *fixation*). If the reduction of the fracture can be accomplished without surgery it is called closed reduction. If a surgical intervention is necessary it is called open reduction. The fixation can be external (cast, external fixator) or internal using plates, screws or wires. Selection of the appropriate method depends on the severity of the fracture as well as the age and physical constitution of the patient.

Plate-osteosynthesis is a method of open reduction and internal fixation used in the treatment of unstable fractures. Wilke et al. found an accelerated recovery for patients with volar plate-osteosynthesis compared to those with external fixation [18]. One or more plates are used to hold screws that are implanted into the bone thereby stabilizing the fracture site. In the case of Colles' fratures it is possible to apply the plate on the dorsal as well as on the volar side of the distal radius. The dorsal approach has long been the main technique, but it can lead to irritation or even rupture of the extensor tendon that runs along the radius dorsally [19]. That is why the volar plate-osteosynthesis has become increasingly common in recent years [20, 21].

The procedure consists of several steps. Once the fracture site is laid open and reduction

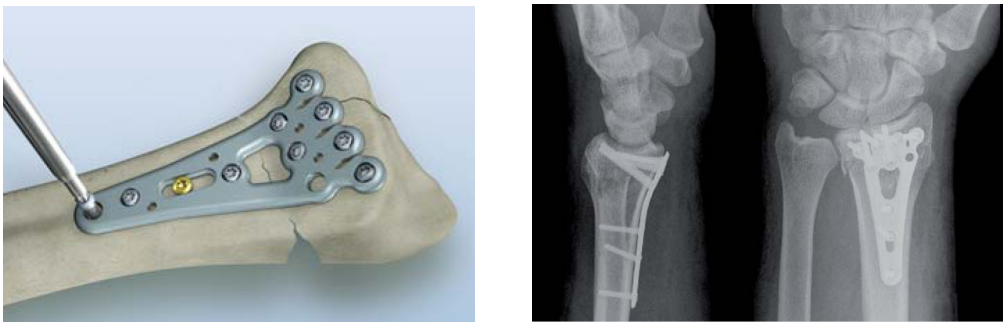

(a) **(b)**

Figure 1.6.: An illustration of a volar plate-osteosynthesis (a) and an X-ray scan of the completed osteosynthesis (b) (source: [17]).

has been accomplished, the anatomically designed plate is positioned on the volar side of the radius and kept in place by Kirschner wires. For each screw a hole is drilled with a diameter smaller than the screw diameter. Then the screw is inserted in the bone. It is important that the tip of the screw reaches the dorsal cortex for maximum hold, but it should not penetrate the cortex to prevent extensor tendon irritation. The screws are equipped with a special head that locks in the plate, thereby creating a fixed-angle connection.

One possible complication associated with osteoporosis is the *secondary loss of reduction*. When an object is gripped with the hand the associated muscle contractions lead to forces that are transmitted through the wrist to the distal radius. Putnam et al. estimate a 1:2.5 ratio of grip force to force transmitted through the distal radius [22]. For an osteosynthesized distal radius with a weakened trabecular structure due to osteoporosis the forces resulting from a gripping with the hand can lead to plastic deformations of trabeculae. This leads to

an axial displacement of the bone fragment and consequently a loss of the reduction. It is suggested that positioning the most distal screws as close as possible to the subchondral bone is beneficial in preventing secondary loss of reduction [21, 23].

1.5. Finite Element Analysis in Biomechanics

Like all biomechanical research, the study of existing osteosynthesis systems and the development of new designs relies on two approaches to investigate the mechanical behaviour of the bone-implant system: the experimental approach using cadaver or artificial bone samples and the simulation approach using numerical tools.
One numerical technique that is applied in all fields of mechanical research and has become increasingly popular in biomechanics is the Finite Element (FE) Method. The construction of the FE meshes is based on data generated by medical imaging tools (CT,MRI,...). Depending on the resolution of the images two main approaches can be distinguished for the FE analysis of bone (Figure 1.7). For the continuum FE approach lower resolution images are used and the microstructure (trabecular network) is homogenized by way of micromechanical modeling. Higher resolution images are the basis of the microFE (μFE) approach that resolves the microstructure with the drawback of bigger models and consequently higher computational demands.

A lot of research has been published relating to the finite element analysis of distal radius

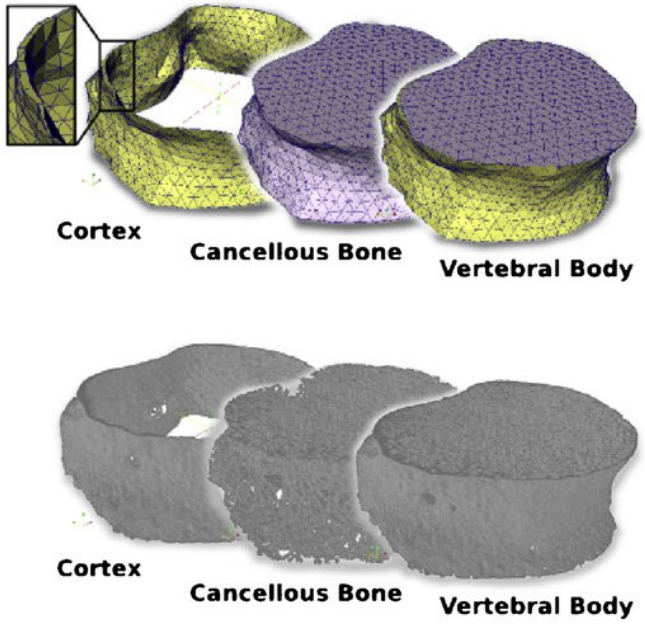

Figure 1.7.: Two FE models of a human vertebra with the continuum FE model on top and the μFE model below (source: [24]).

fractures as well as the mechanical interaction of implants and bone. Varga et al. have applied finite element models to improve the established methods used to predict the risk for Colles' fractures [25]. The mechanics of a titanium screw implanted into a sheep vertebra and subjected to axial tension have been studied by Wirth et al. in [26]. The displacement of a polymer screw in a human femur head under axial compression has been analysed and

compared to mechancial experiments in [27]. Both studies used generic load cases, that do not represent the loading of an in-vivo implant.

1.6. Aim of this Thesis

Based on the osteosynthesized distal radius under axial loading as a clinically relevant example, this thesis examines the different steps necessary to generate linear μFE models of a bone-screw system using data obtained from CT scans. It tries to address issues associated with image generation and processing as well as FE modeling, analysis and post-processing. The results from the numerical models are compared with a mechanical test.

2. Methods

The following chapter introduces the methods used in the context of this thesis in two parts. The first part explains the mechanical test. It starts with a stepwise description of the sample preparation and the CT scanning procedure. Then the setup of the mechanical test is presented. The second part concerns the FE analysis. It introduces the methods applied in the image processing of the CT data and the generation of the FE models.

As mentioned before, the volar plate-osteosynthesis is the starting point and inspiration for this study of a bone/screw connection. Modelling the whole implant system would, however, exceed the realms of possibility in terms of mechanical testing as well as FE simulation. To reduce the complexity of the problem the following simplifications are made:

- The volar plate-osteosynthesis consists of a plate and several locking screws. Such a configuration would increase metal artifacts in the CT images as well as FE model size significantly. This leads to the decision to use only one screw and disregard the plate completely.
- The investigated area of the radius is restricted to a cuboid region cut from the distal part (yellow region in Figure 2.1).
- The complex loading in the real structure (Figure 2.1, left) was simplified by a unidirectional load acting on the screw head to represent the major loading of a bone screw (Figure 2.1, right).
- The problem is simulated with a linear FE model that assumes linear elastic material, small deformations and perfect bonding.

As this thesis is aimed at the definition of the pre-processing and modeling aspects of a μFE analysis and not at a quantitative comparison of experimental and simulation results, it was decided that one sample would be sufficient to demonstrate the different aspects of the modeling process. Therefore, 4 samples were prepared for the mechanical test to ensure one valid data set, but in the end only the data of Sample3 was used to generate the FE models.

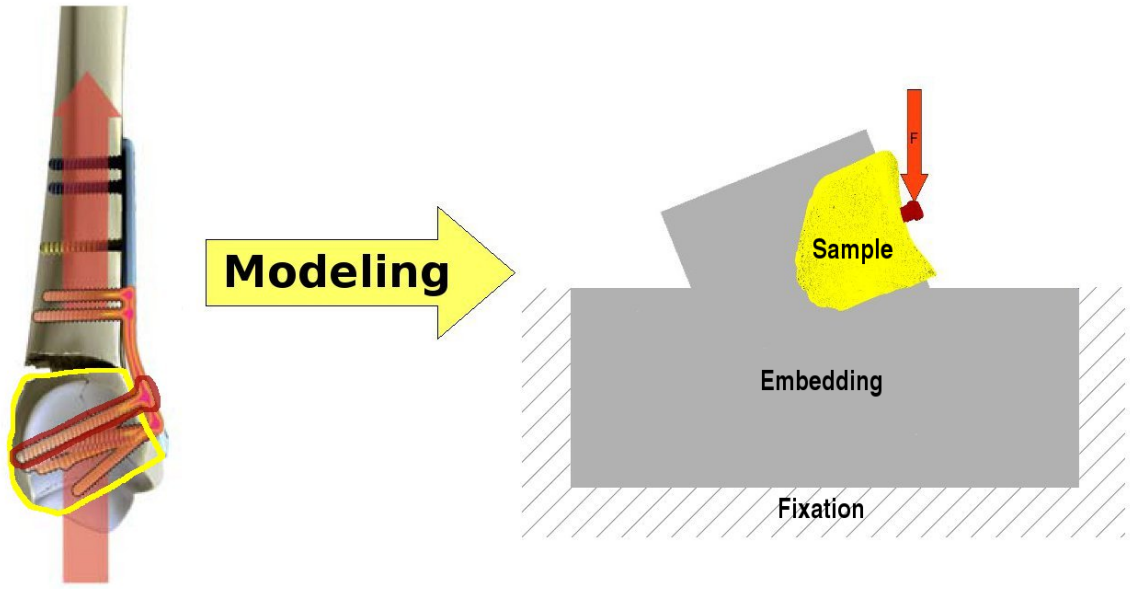

Figure 2.1.: Derivation of the model for experiment and FE analysis (left figure taken from [28]).

2.1. Mechanical Test

For the mechanical test of the screw-bone interaction under general loading 2 pairs of distal radii were investigated. They came from the anatomy institute of the AKH Wien and were taken from two female donors (48 and 93 years old). Before preparation and between individual steps of the preparation the bones were stored in a freezer at the laboratory of the ILSB at -20 degree celsius. Figure 2.2 gives an overview of the different preparation steps described in the following sections.

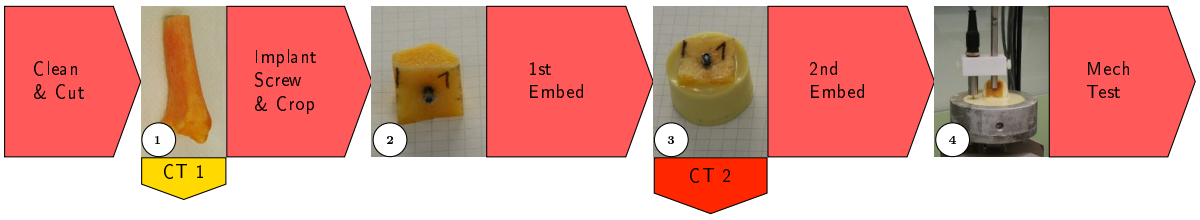

Figure 2.2.: A flow chart of the different steps taken in preparation of the mechanical test

2.1.1. Preparation of the Sample

Each sample was unfrozen for at least 4 hours at room temperature and carefully cleaned from soft tissue (muscle, tendons, articular cartilage). This was done because the presence of soft tissue can hinder the bonding between embedding and bone (see Section 2.1.6) and it can also complicate the segmentation of the CT images (see Section 2.2.4). To fit the dimensions of the cylindrical CT sample holder (diameter 36.9 mm, length 80 mm) the bones were then

cut with a hand saw to a length of about 60 mm from the distal joint. Figure 2.3a shows a cleaned and cut sample.

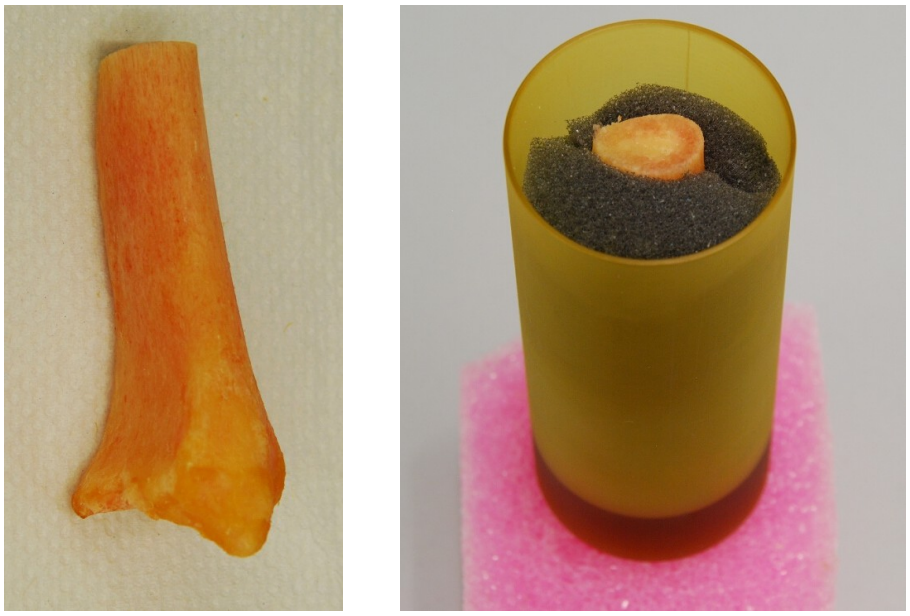

(a) (b)

Figure 2.3.: A distal radius sample after cleaning and cutting (a) and the same sample in the CT sample holder surrounded by spongy material for fixation (b).

2.1.2. Computed Tomography

The samples were individually placed in the sample holder and padded with spongy material to prevent movement during the CT scanning process (Figure 2.3b). The scanning was done with a Micro-CT system (μCT 40, Scanco Medical AG, Switzerland). The highest possible resolution of for this sample size (18 μm) was chosen and the samples were scanned in air. The settings used for the scan were: 70 kVp, 114 μA and an integration time of 300 ms. After the scan the samples were frozen again.
No motion artifacts were visible in the resulting images. The initial resolution of 18 μm proved to be computationally not feasible. Therefore, the voxel size was reduced to 36 μm.

2.1.3. Implantation of the Screw

A locking screw manufactured by MEDARTIS [28] was used for the mechanical test (Figure 2.4). It is specifically designed for volar osteosynthesis with fixed-angle plating (see Section 1.4) and made out of grade 4 titanium. The screw has a hexadrive screw head (similar to Torx®) and a double threaded profile with self-tapping capabilities.
The implantation of the screw (length 20 mm, ∅2.5 mm) was performed by a surgeon with experience in plate-osteosynthesis. The radius sample was fixed in a grip. A pilot hole of 2 mm diameter was drilled through the bone in volar-dorsal direction perpendicular to the bone surface with an electrical drill. The screw was implanted using a manual screw driver. It was made sure that one of the threadless sides of the screw head was oriented in proximal

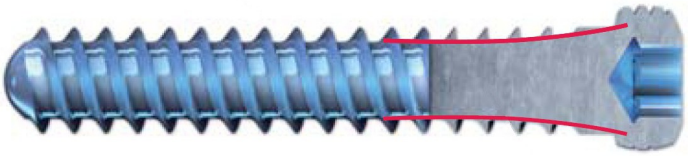

Figure 2.4.: A sketch of the locking screw used in this test (source: [28]).

direction (see Section 2.1.4) and that the tip of the screw reached the dorsal cortex. A magnified view of the screw head is shown in Figure 2.5b. Due to the osteoporotic nature of the bone samples, one screw got misaligned during the implantation process and deviated from the drilled direction (Sample2). This sample was excluded from the test.

2.1.4. Definition of the Area of Force Application

Well defined boundary conditions are important for the controlled execution of the experiment as well as for the subsequent finite element modeling. As the sides of the screw head are slightly convex, a flat surface had to be created to ensure a predictable force transfer to the screw. For this the sample was fixed in a grip with the bone axis in vertical direction. A hand held rotary tool equipped with a grinding stone (Dremel Corp., USA) was used to carefully produce a flat area on the screw head perpendicular to the bone axis (Figure 2.5b).

2.1.5. Cutting of the Samples

The samples were cut with a band saw (300CP/R, Exakt Vertriebs GMBH, Germany). The desired cutting edges were drawn on the sample with permanent marker. The bone was gripped in the machine and fixed so that the orientation of the screw axis was parallel to the blade of the band saw (Figure 2.5a). Then 4 cuts were performed (lateral, medial, distal, proximal) resulting in a $\sim$20 mm $\times$ $\sim$20 mm $\times$ h bone sample, where h is the volar-dorsal distance, which differs for each sample (Figure 2.6). The screw penetrates the dorsal cortex in the center of the 20 mm x 20 mm surface. During the cutting process the blade of the saw was cooled with a constant flow of water to minimize the heat transfer into the bone.

For one specimen (Sample3) the pivoting angle of the grip was not sufficent to perform the distal and proximal cut. Therefore, this sample had to be put in a different grip and manually cut with a hand saw. After cutting, the samples were frozen again.

2.1.6. First Embedding of the Samples

The bone samples were unfrozen at room temperature and dried with paper towels. The samples were put on a plate made of teflon with the screw in vertical orientation (Figure 2.7a). A small amount of plasticine was used to keep the samples in the desired position as well as to surround the tip of the screw penetrating the dorsal cortex and thereby preventing the embedding material from reaching the tip of the screw. Small plastic rings (inner diameter 32 mm, height 35 mm) were placed on the plate so that the samples were in the center (Figure

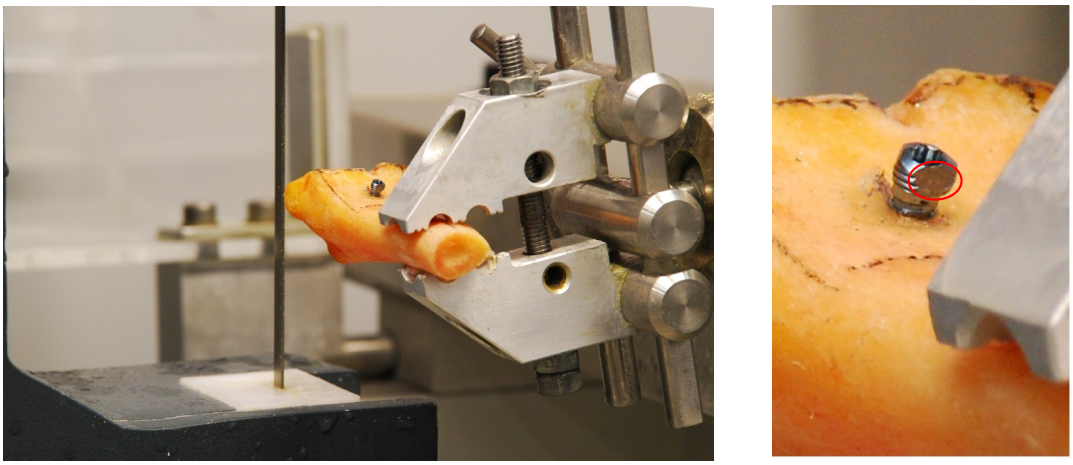

(a) (b)

Figure 2.5.: One sample in the grip of the Exact band saw (a) and a detail showing the flat surface on the screw head (marked in red) (b).

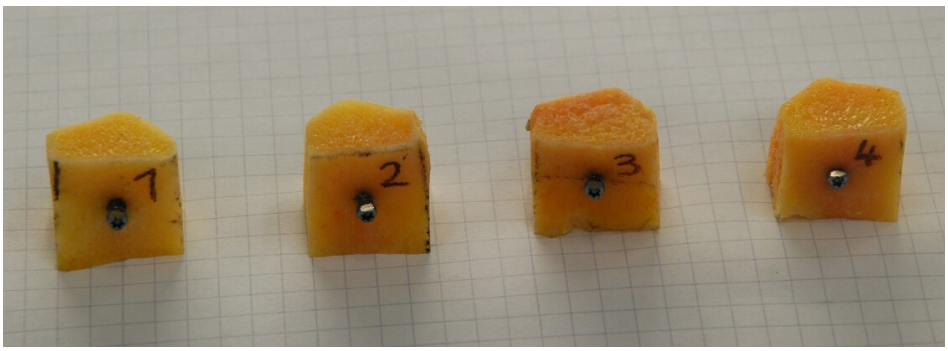

Figure 2.6.: The samples after cutting with the Exact band saw.

2.7b). The rings were lined with plasticine at the bottom to make them stick to the teflon plate and to keep the embedding material from running out.
Then the embedding material was prepared. A polyurethan material (PUR 145, FWD HGmbH, Austria) was used by mixing two liquid components (a matrix and a hardening agent, 1:1 in weight). Hardening time was ∼15 minutes. As this embedding material has an x-ray attenuation coefficient close to bone marrow, glass fibres were added to ensure visibility of the embedding in the CT images. Following a previous test [29], the weight ratio of fibres to matrix to hardening agent was chosen to be 2:5:5. First the fibres were mixed into the hardening agent and stirred for 5 minutes to ensure a uniform distribution of the particles. The matrix was added and the mixture was stirred for 1 minute and 15 seconds before being put into the mold (Figure 2.8a). As the gap between the sample and the surrounding ring was only a few millimeters wide, a 50 ml syringe was used to put the embedding material into the mold. To reduce the formation of air bubbles close to the bone three layers of embedding material were injected.

After the material was hardened, the samples were cut out of the plastic molds and the

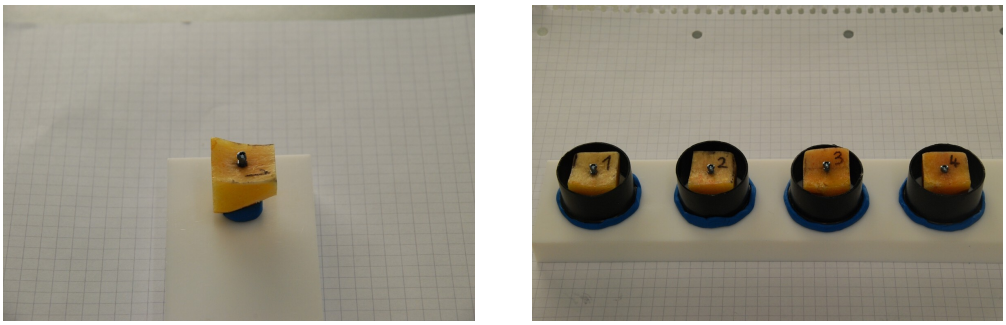

(a) **(b)**

Figure 2.7.: A sample fixed to the teflon plate with a piece of blue plasticine (a) and the setup before the embedding material was filled into the mold (b).

plasticine was removed as carefully as possible (only a small amount of plasticine was left, covering again the tip of the screw penetrating the dorsal cortex). Afterwards, the samples were placed upside down in a similar mold as before, again with the screw in a vertical position. Embedding material was poured into the mold to fill the hole and create a flat surface on the bottom. The finished samples (Figure 2.8b) were then scanned using the procedure described in Section 2.1.2.

2.1.7. Second Embedding and Setup of Mechanical Test

The testing of the screw was carried out on a servohydraulic testing machine (MiniBionix 858, MTS Systems Corporation, USA), from hereon simply called MTS. The load was applied via a cylindrical steel rod ($\varnothing 8\ mm$) fixed in the upper grip of the MTS. Great care had to be taken to align the flat surface on the screw head and the flat surface of the rod parallely, due to the relatively small dimensions of the area where the force was applied (1-2 mm^2). Therefore, the second embedding was performed directly on the MTS following these steps:

1. A metal form was fixed in the lower grip of the MTS and coated with separation spray on the inside to ensure easy removal of the sample after the mechanical test.

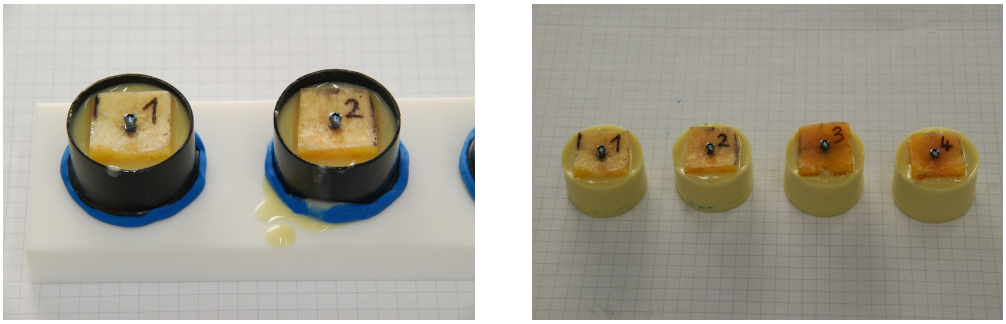

(a) (b)

Figure 2.8.: The embedded sample still in the mold (a) and the finished first embedding (b).

2. Three holes (2,2 mm in diameter, ∼3 mm in depth) were drilled into the cylindrical surface of the first embedding of the sample using an electrical drill. Then metal screws (∅2,5 mm) were screwed into the holes to a depth of ∼5 mm forming a tripod (Figure 2.9a). The screws provided a stable support for the positioning of the sample in the mold and gave the sample a better purchase in the second embedding.

3. The sample was positioned in the form with plasticine holders stuck to each screw head to fix it in the form during embedding (Figure 2.9a).

4. The steel rod was lowered until it nearly touched the screw head. Using a small light source to better see the gap between rod and screw head, the sample was manipulated until no gap between the flat surfaces of the loading cylinder and the screw head was visible anymore.

5. A plastic cylinder coated with separation spray was also positioned in the form (Figure 2.9b) to generate a hole in the embedding for a linear variable differential transformer (LVDT, see explanation below).

6. 130 mg of PUR 145 embedding were prepared (according to the procedure defined in Section 2.1.6) and carefully poured into the form. After one hour the embedding was assumed to be completely hardened and ready for testing.

The vertical translation of the steel rod was controlled with the crosshead of the MTS. The internal sensors of the system were used to record the force and the displacement applied during the test. To make sure that the compliance of the MTS does not influence the final output, an external LVDT was used to provide additional displacement data. This sensor was attached directly to the steel rod with a teflon grip (Figure 2.10) and connected to an external acquisition system (Spider8, HBH, Germany). Data was acquired at 50 Hz.

The test procedure was performed in 2 steps, a pre-loading step and a measuring step. In the pre-loading step the steel rod was lowered in 10 μm increments onto the screw head until the force sensor of the MTS reported a pre-load of 10 N. This position was then used as the zero displacement level for both the MTS and the external LVDT. In the measuring step, the steel rod was displaced with a constant rate of 5 mm/min until a maximum displacement of 2 mm

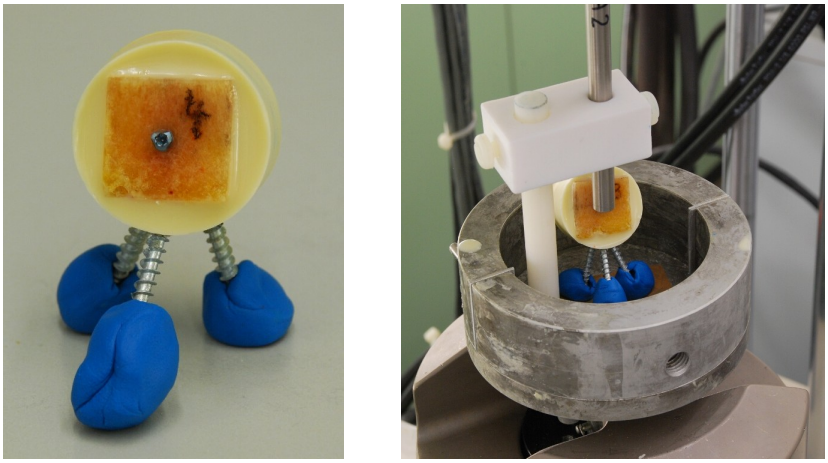

(a) (b)

Figure 2.9.: The sample with the three screws inserted (a) and the testing setup right before the second embedding was applied (b).

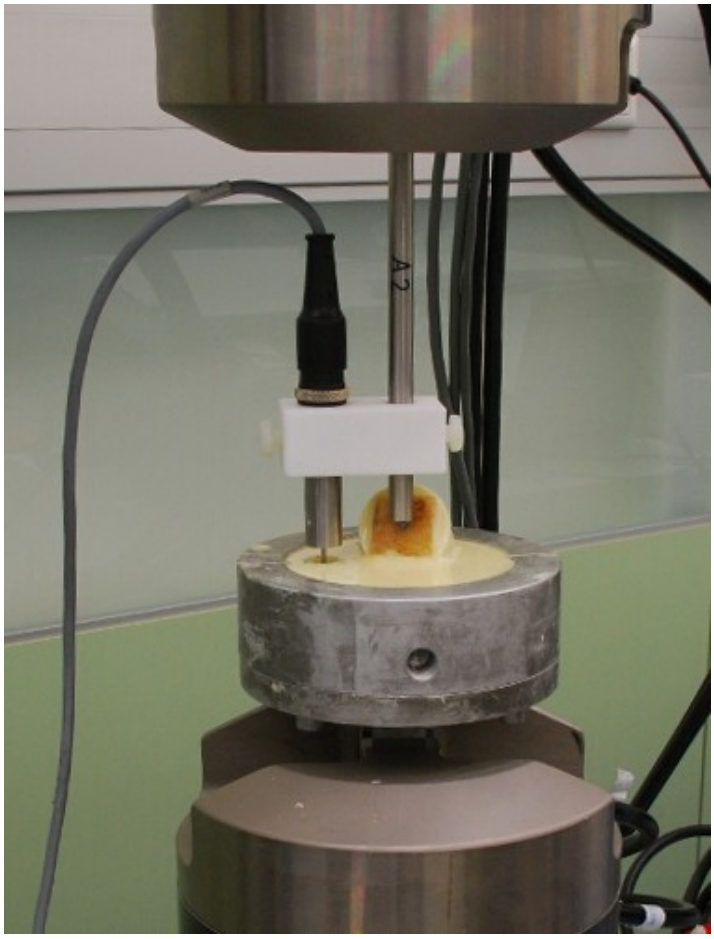

Figure 2.10.: The sample with the 2nd embedding applied before the start of the mechanical test.

was reached. The resulting force-displacement data from the MTS as well as the displacement data from the external LVDT were recorded and saved digitally.

2.2. Finite Element Analysis

The aquired CT-data (see Section 2.1.2 and 2.1.6) was used to generate finite element meshes. The following chapters describe the different steps taken to setup the FE-models. The following abbreviations are used from here on: The CT image of the distal radius before implantation of the screw is referred to as *noScrew*. The CT image of the sample after the implantation and the first embedding is called *realScrew*. The segmented image of the distal radius with the screw virtually inserted is called *virtScrew*.
Five different models were generated. The three models derived from the CT image after implantation of the screw are

- *realScrew*: perfect bonding between screw and bone,
- *realScrew_noT*: no tension is transferred at the bone / screw interface
- *realScrew_noBT*: no tension is transferred at the bone / screw interface and the trabeculae that were broken in the implantation process are removed.

The two models derived from the CT image before implantation by virtually inserting the screw are

- *virtScrew*: perfect bonding between virtually inserted screw and bone and
- *virtScrew_noT*: no tension is transferred at the bone/screw interface.

These two models are generated by combining the image of *noScrew* with the image of the screw extracted from *realScrew*. Therefore, they do not contain broken trabeculae by default. The pre-processing steps necessary to generate these five models are presented as a flow chart in Figure 2.11 and described in detail in the following chapters (bold numbers in parentheses in the text refer to the numbered modeling steps depicted in the flow chart).

2.2.1. Registration

The diagnosis of diseases and the preparation of medical procedures relies heavily on data aquired by different means of image production (CT, MRI, ...). To compare two images taken at the same anatomical site but at different times (e.g. before and after implantation) or with different imaging techniques, it is important to spatially align the different images with each other. This is achieved in an iterative procedure called registration. One image is kept fixed while the second is rotated and translated step-wise. For each registration step a metric is calculated, which quantifies the misalignment between the two images. From this metric a new registration step is derived. The process stops when the metric falls below a user defined value.
In the context of this thesis, registration **(13)** was used to align *noScrew* **(12)** with *realScrew* **(2)**. This was necessary

- to see how the implantation procedure effects the area around the screw (trabeculae get broken and dislocated),
- to use *noScrew* as a contour mask to remove the plasticine near the tip of the screw from *realScrew* due to the fact that plasticine has CT gray values within the range of the gray values of bone,

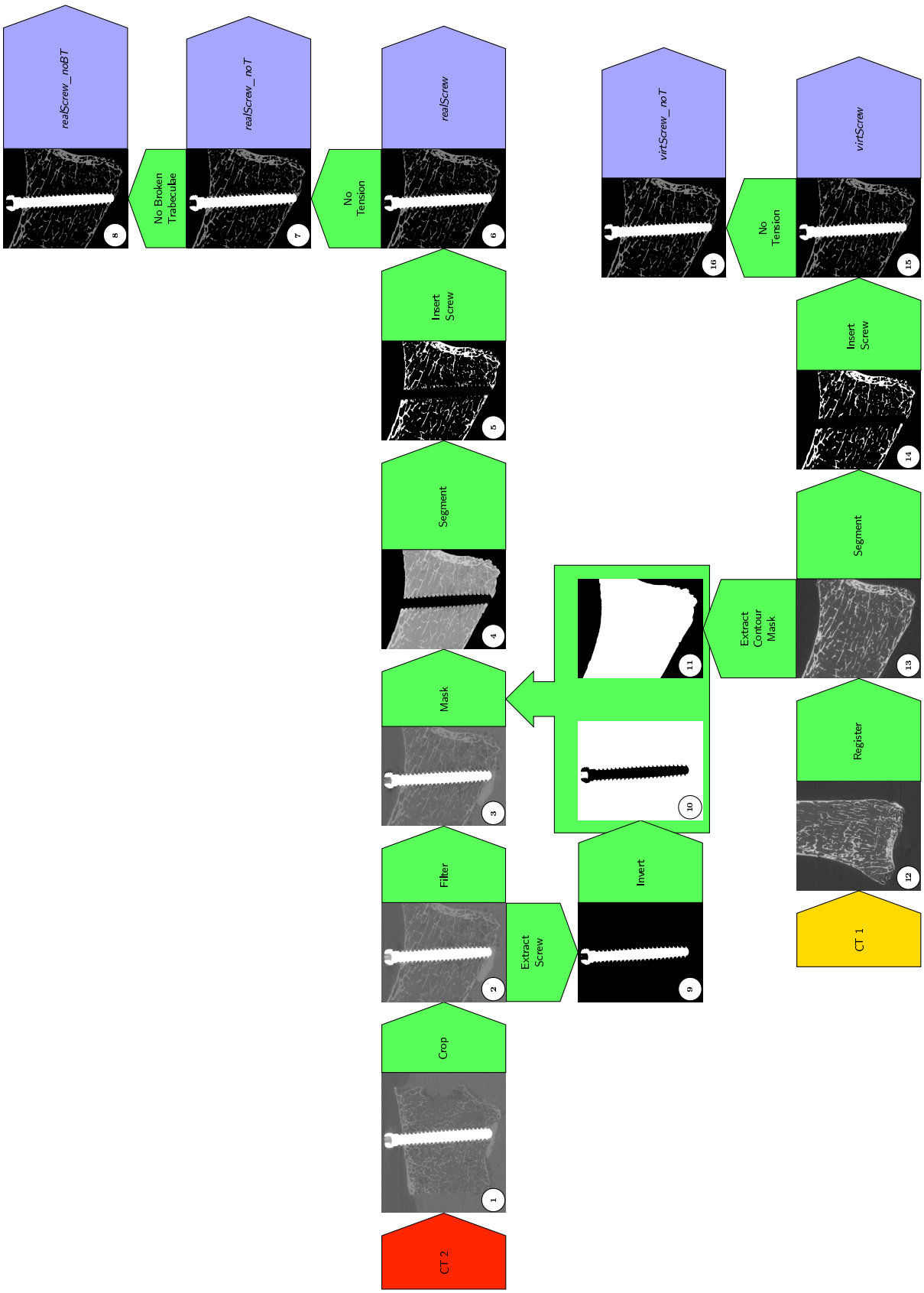

Figure 2.11.: Flow chart of the FE preprocessing

- to virtually insert the image of the screw into *noScrew* to generate *virtScrew* and
- to mask broken trabeculae by computing the difference between *realScrew* and *virtScrew*.

The registration was done in Medtool (an in-house shell script manager for image processing and FE mesh generation developed by Dr. Dieter Pahr at the ILSB) using scripts from the open-source C++ library 'Insight Segmentation and Registration Toolkit' (ITK) (Kitware Inc., USA) [30]. The *realScrew* model was used as the fixed reference image, *noScrew* as the moving image. To facilitate the automatic registration process *noScrew* was first rotated and translated to have roughly the same orientation as the reference. Then a cuboidal piece was cut from each image in such a way that the piece from the moving image contains the same part of the sample as the piece from the fixed image. The piece from the fixed image had dimensions of 3.24 x 5.4 x 2.7 mm (Figure 2.12), while the piece from the moving image was chosen with slightly bigger dimensions (4.32 x 6.48 x 3.78 mm). These two pieces were then registered using the mutual information metric by Mattes [31] and a gradient descent optimizer to minimize the metric. This process took 208 s for the 36 μm model and 64 s for the 54 μm model on two Intel Core2 Duo 2.66GHz CPUs with 8GB memory each. The script gives the center of rotation, the rotations and the translations applied during registration. These were subsequently applied to the whole *noScrew* image to align it with *realScrew*. Finally the 36 μm and the 54 μm versions of the *realScrew* and the registered *noScrew* model were cropped to the same size. The 72 μm versions were created by recoarsening the finished 36 μm models.

As the registration is an iterative process a residual difference between the fixed and the moving image will always remain. This offset is quantitatively small and visually not noticeable in the small cuboid region. But when the rotations and translations are applied to the whole sample, the difference is propagated and becomes visually noticeable as a misalignment between *realScrew* and the registered *noScrew*. Figure 2.19 illustrates this on a slice through the model. The areas marked with red circles show examples of deviations in microarchitectural structure between *realScrew* and *noScrew*. These differences are also visible in the segmented images. As the CT image is constrained to a voxel grid where each voxel has a constant value the rotations and translations applied during the registration process of *noScrew* make it necessary to interpolate the data. This leads to a deterioration of the image quality in the form of blurring (Figure 2.13).

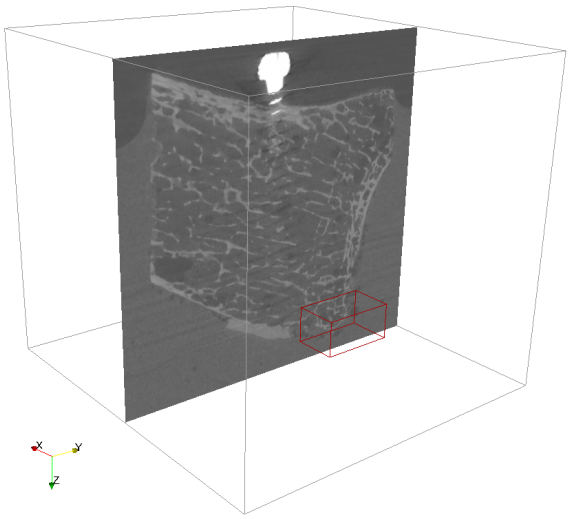

Figure 2.12.: The cuboid region (dark red) that was used for the registration of *noScrew* in relation to *realScrew* (grey outline).

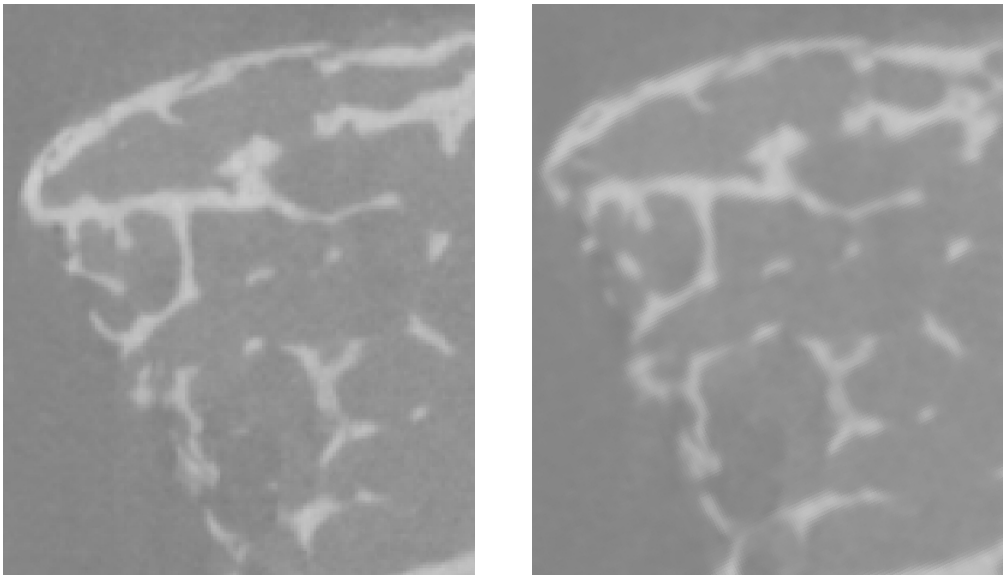

(a) **(b)**

Figure 2.13.: A magnified section of the 36 μm version of *noScrew* before (a) and after registration (b). One can see a loss in overall sharpness due to the effect of interpolation applied during the registration process.

2.2.2. Histograms

To illustrate the distribution of voxel values in the sample histograms were generated. They give the amount of equally valued voxels for each voxel value. Comparing the histograms of *realScrew* and the registered *noScrew* shows the differences between the two configurations (Figure 2.14). The histogram for *realScrew* has four peaks corresponding (in order of voxel value) to air, embedding and marrow, bone and plasticine, and screw. The one for *noScrew* shows only three peaks, two distinct ones for air and marrow and a weakly pronounced one for bone.

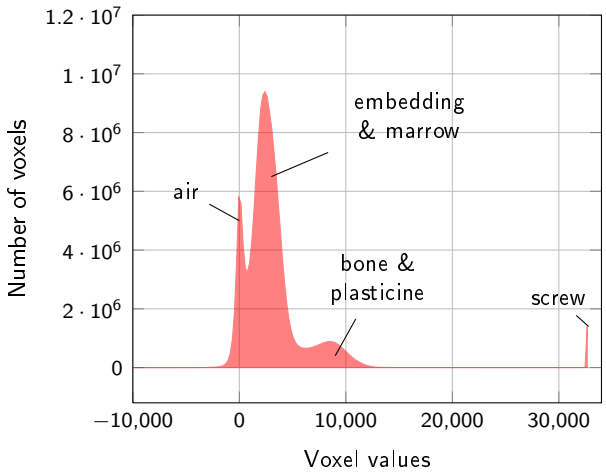

(a) *realScrew*

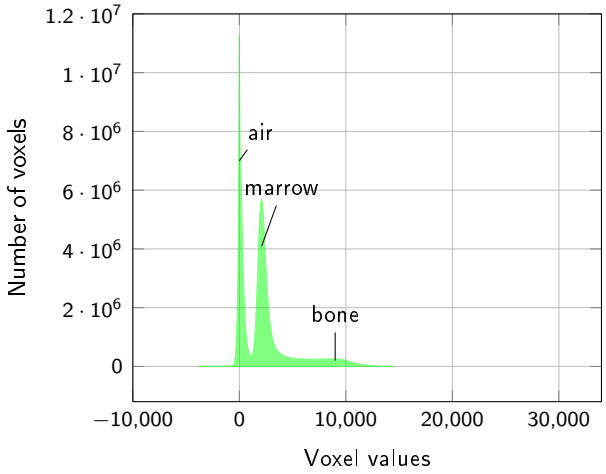

(b) *noScrew*

Figure 2.14.: Histograms of the 36 μm version of *realScrew* (red) and *noScrew* (green).

2.2.3. Metal Artifact Reduction

The presence of the titanium screw in *realScrew* leads to severe artifacts in the CT data due to the high density of the metal. Concentric streaks and darkended areas can be seen, as well

as brightening around the screw (Figure 2.15). This causes significant problems during the segmentation process. A matlab script based on an existing code contributed by the Com-

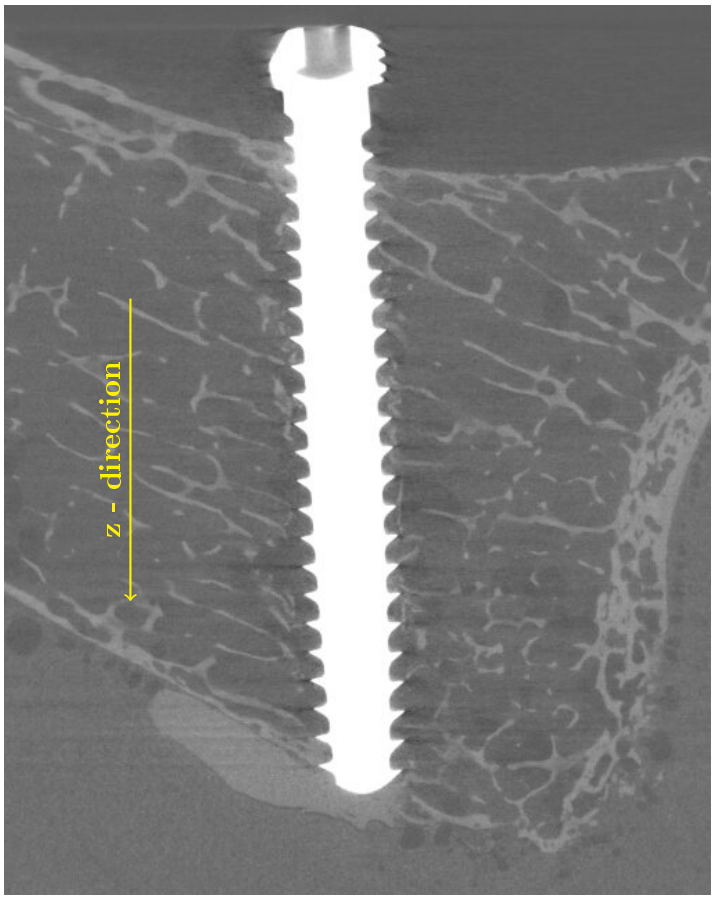

Figure 2.15.: Metal artifacts in the CT scan due to the titanium screw. Notice the brightened areas near the screw and the horizontal darkened streaks at the tips of the thread.

putational Image Analysis and Radiology Laboratory (CIR) at the Allgemeines Krankenhaus (AKH) Wien was used to reduce these artifacts in the vicinity of the screw. As this script reads 8-bit data the *realScrew* data had to be scaled to a gray value range of 0 to 255. The CT data is separated into slices along the z-axis of the sample, which corresponds roughly with the axis of the screw (Figure 2.15). The metal artifact reduction algorithm is then applied individually to each slice according to the following procedure.

First all screw voxels (highest grey value) are identified. Then the distance d to the nearest screw voxel is calculated for all other voxels. It is assumed that the influence of the screw will be the same on all voxels that have the same distance d from the screw. Thus for the i voxels with the same distance d and the grey values $x_{d,i}$ the mean of the grey values

$$\bar{x}_d = \frac{\sum_i x_{d,i}}{i}$$

is calculated. This mean value decreases with the distance from the screw as the influence of the screw on the voxel grey values also decreases. A distance d_{base} can be identified were the screw has no more artifactual influence on the voxels. The mean over all voxels at d_{base} is called the baseline value $\bar{x}_{base}$. Finally, the reduced grey values

$$x_{d,i}^{red} = x_{d,i} - (\bar{x}_d - \bar{x}_{base})$$

are calculated for all voxels with $d \leq d_{base}$. The reduction of the titanium induced glow in the filtered image **(3)** is shown in Figure 2.16.

For this study d_{base} was found by trial and error to be 3.122 mm. As the MATLAB script counts the distance d in voxels, d_{base} values of 52, 39 and 26 were chosen for the 36 μm, 54 μm and 72 μm meshes respectively. Figure 2.17 shows the effect of the metal artifact reduction script on the segmented image. The unfiltered image gives a pronounced ring of bone material around the screw (Figure 2.17b) that does not correspond with the CT image (Figure 2.17a). The filtered image (Figure 2.17c) gives a much better representation of the peri-implant region. Areas outside the radius chosen for the script are not affected by the filter. For the source code of the script see appendix A.

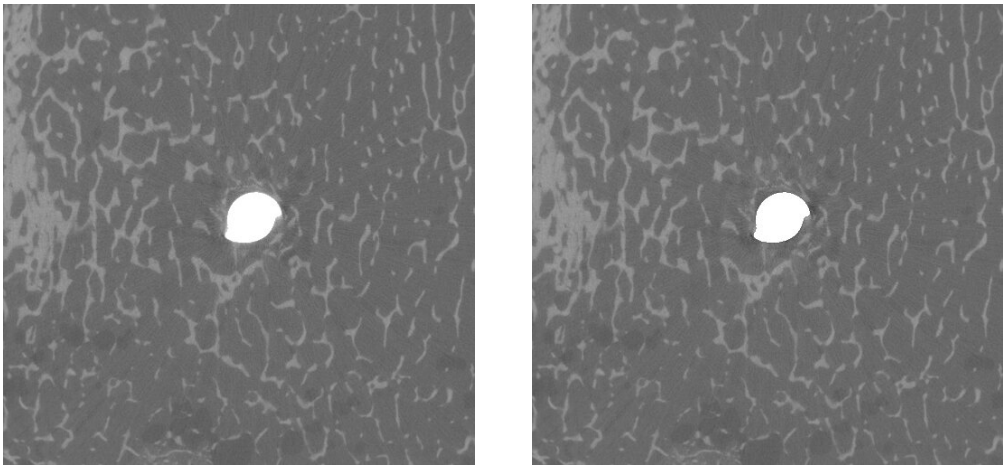

(a) **(b)**

Figure 2.16.: A slice of *realScrew* before (a) and after metal artifact reduction (b).

2.2.4. Segmentation

In the CT image each material in the sample is represented by an (overlapping) range of grey values (see Section 2.2.2). In the segmentation process each material is assigned one distinct grey value, that will correspond to an element property in the FE model. The "threshold" script in Medtool was used for this task. This function compares all grey values in the image to a user-defined threshold value. Those voxels with grey values smaller than the threshold are set to zero, those with higher grey values are set to the threshold value.
The segmentation process had to be divided into individual steps for several reasons:

- The screw has to be extracted from *realScrew* to be inserted into *noScrew* after the segmentation.

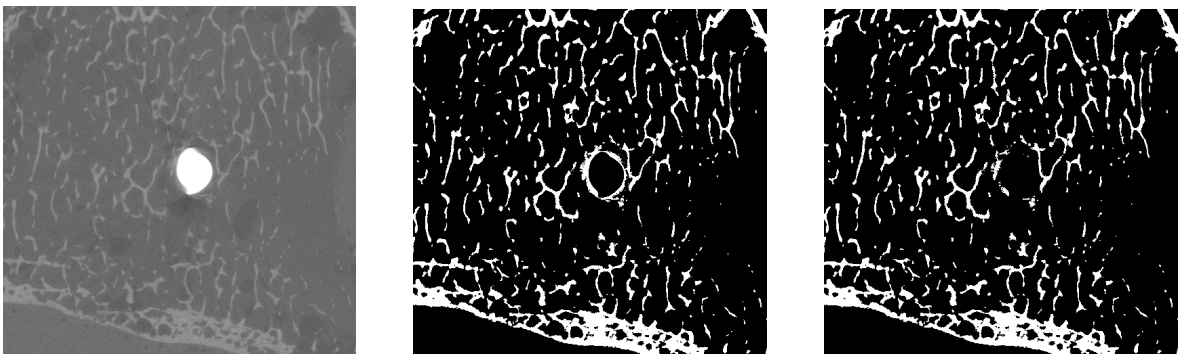

(a) (b) (c)

Figure 2.17.: The z-midplanes of the *realScrew* CT image at 36μm (a) as well as of the segmented *realScrew* at 36μm before (b) and after metal artifact reduction (c). The screw was masked from the segmented images.

- The *realScrew* image includes 5 different materials (titanium, bone, marrow, embedding and plasticine), where only titanium and bone are included in the FE model.
- The trabecular structure in the segmented images of *realScrew* and *noScrew* should be as similar as possible.

To extract the screw the lowest grey value of the screw found in the histogram was chosen as the threshold, which removes all other materials from the image (i.e. setting their grey values to zero) **(9)**.
To remove the embedding and the plasticine at the screw tip, a contour mask **(11)** was generated from *noScrew* with the "fill" function in Medtool, which uses a region growing algorithm to fill the inside of the bone with voxels of a single defined gray value. Applying this mask and a mask of the screw **(10)** to the *realScrew* data gives an image that only includes bone and marrow **(4)**.
Then thresholds had to be found for the *realScrew* and the registered *noScrew* models at 3 different resolutions (36μm, 54μm and 72μm). A cuboid region of trabecular bone (5.4 x 7.56 x 7.2 mm) was cut from each model at a location outside of the baseline distance d_{base} determined in section 2.2.3 (Figure 2.18). Starting with the 36μm configuration the thresholds for the *realScrew* and *noScrew* models were selected by matching the ratio of bone to total volume (BVTV). Visual comparison was used additionally to make sure that the segmented images corresponded to the CT images as closely as possible. Once the thresholds for the 36μm models were found the thresholds for the 2 other resolutions were matched by visual comparison with the respective CT image as well as the segmented 36μm model. Table 2.1 lists all thresholds that were derived from this process. The *virtScrew* data was used with the unscaled voxel values range to make it easier to fine tune the threshold. The threshold decreases with growing voxel size because the merging of voxels that is associated with a resolution change lowers the voxel values of the image on average. The resolution change is also responsible for the increased BVTV as small microachitectural features like pores in the cortical bone are lost in the coarser image. The values derived from the cuboid region were than used as global thresholds for the masked *realScrew* **(5)** and *noScrew* models **(14)**.
Finally the screw was added to *realScrew* **(6)** and *noScrew* **(15)** and the segmented data was

scaled to grey values for bone and screw voxels of 1 and 2, respectively.

Finding a satisfying threshold for the *realScrew* model presented several challenges. First, the procedure used to reduce the metal artifacts (see Section 2.2.3) did not completely eliminate the glow around the screw. Therefore, the chosen threshold was a compromise between an over-estimation of the trabecular structure near the screw and an under-estimation away from the screw. Second, to be able to compare *realScrew* and *virtScrew* results it was important for the segmented images to be as similar as possible. This was done by visual inspection and by comparing the BVTVs of a trabecular region cropped from the same region from both images. Third, to be able to compare different voxel sizes the resulting images had to be as similar as possible. This was also done by visual inspection.
Comparing the segmented image of *realScrew* with the CT image of *realScrew* shows several deviations in the segmented image:

- Pores in the cortical bone are smaller or altogether closed,
- Trabecular connectivity is lost,
- Trabecular connectivity is exaggerated,
- Trabeculae are thicker than they are in the CT image.

Comparing the segmented images of *realScrew* and *virtScrew* shows several differences in terms of microarchitectural bone structure (Figure 2.19). While the overall alignment between the two images is good, differences in trabecular connectivity can be seen in several places. There are instances of connected trabeculae in *realScrew* that are not connected in *virtScrew* and vice versa.

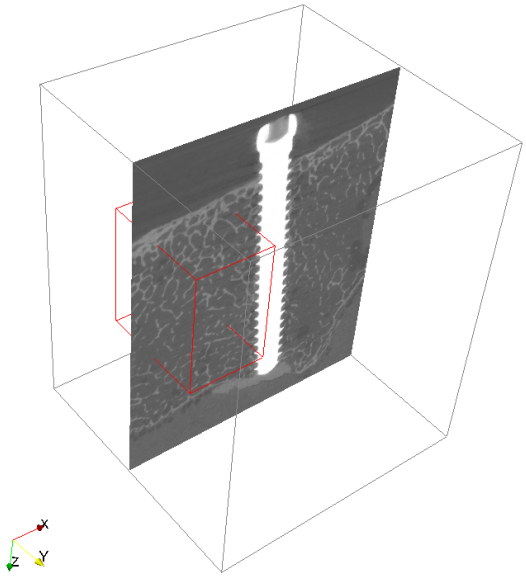

Figure 2.18.: The cuboid region that was used to calibrate the segmentation threshold of the *realScrew* and *virtScrew* models.

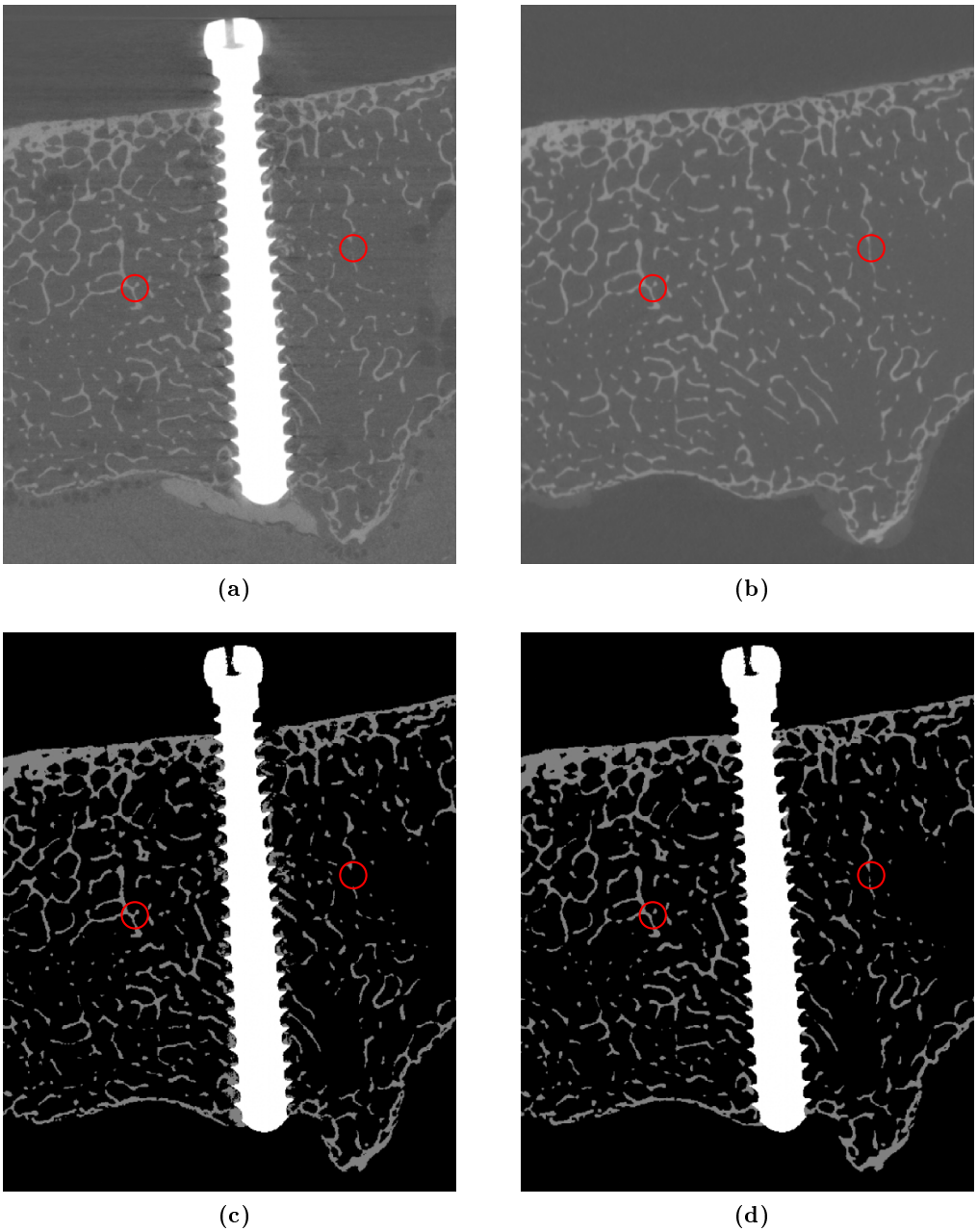

Figure 2.19.: The y-midplanes of the CT image of *realScrew* (a) and *virtScrew* (b) at 36μm as well as of the corresponding segmented models at 36μm (c) and (d). Red circles mark examples of differences in microarchitectural details in the two CT images and the segmented data.

	realScrew		*noScrew*	
Voxel Size (μm)	Threshold	BVTV (%)	Threshold	BVTV (%)
36	122	12.334	5685	12.336
54	113	12.726	5498	12.725
72	104	13.338	5320	13.331

Table 2.1.: Tresholds and resulting BVTV for a cuboid trabecular region taken from *realScrew* and *noScrew*.

No Tension

The linear model produced by the voxel conversion creates a perfectly bonded interface between screw and bone. This however is not a realistic representation because it allows the transmission of tensile forces across the interface. Therefore, the first layer of bone voxels on the tension side of the screw was deleted leaving a small gap where no forces can be transmitted (Figure 2.20). This was achieved by dilating the screw by one voxel using the morphological filter in Medtool and applying it as a mask to the bone voxels on the tension side of the interface. This procedure was applied to the *realScrew* and the *virtScrew* data. To remove as little bone as possible from the model the smallest possible gap of one voxel length was chosen. This however resulted in different physical gap sizes for different voxel sizes. The longer the voxel length, the more bone is removed and the bigger is the resulting gap. From here on the resulting models are called $realScrew\_noT\mathbf{(7)}$ and $virtScrew\_noT\mathbf{(16)}$, respectively.

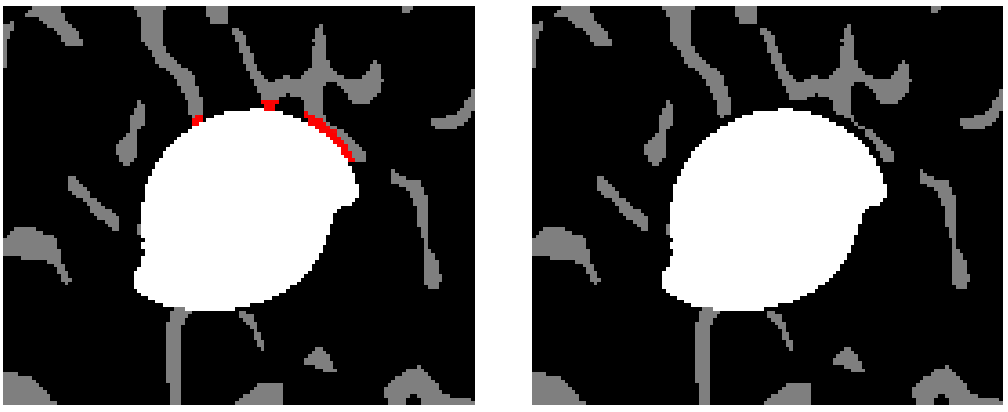

(a) **(b)**

Figure 2.20.: A magnified view of the segmented image before (a) and after removal of voxels on the tension side of the screw (b). The voxels that are removed are marked in red.

No Broken Trabeculae

The drilling of the hole and the insertion of the screw leads to the fracture, deformation and dislocation of trabeculae. These trabecular fragments remain in the area around the screw, but it can be assumed that they do not contribute to the load bearing capabilities of the

bone. The resolution of the CT scan is not high enough to differentiate the broken from the connected trabeculae in the segmentation and the broken trabeculae appear connected with the rest of the model.
To identify these broken trabeculae in the model, *noScrew* was subtracted from *realScrew*. The remaining bone voxel were assumed to be broken and masked from the *realScrew* model (Figure 2.21). The resulting model **(8)** is called *realScrew_noBT* in the following chapters.

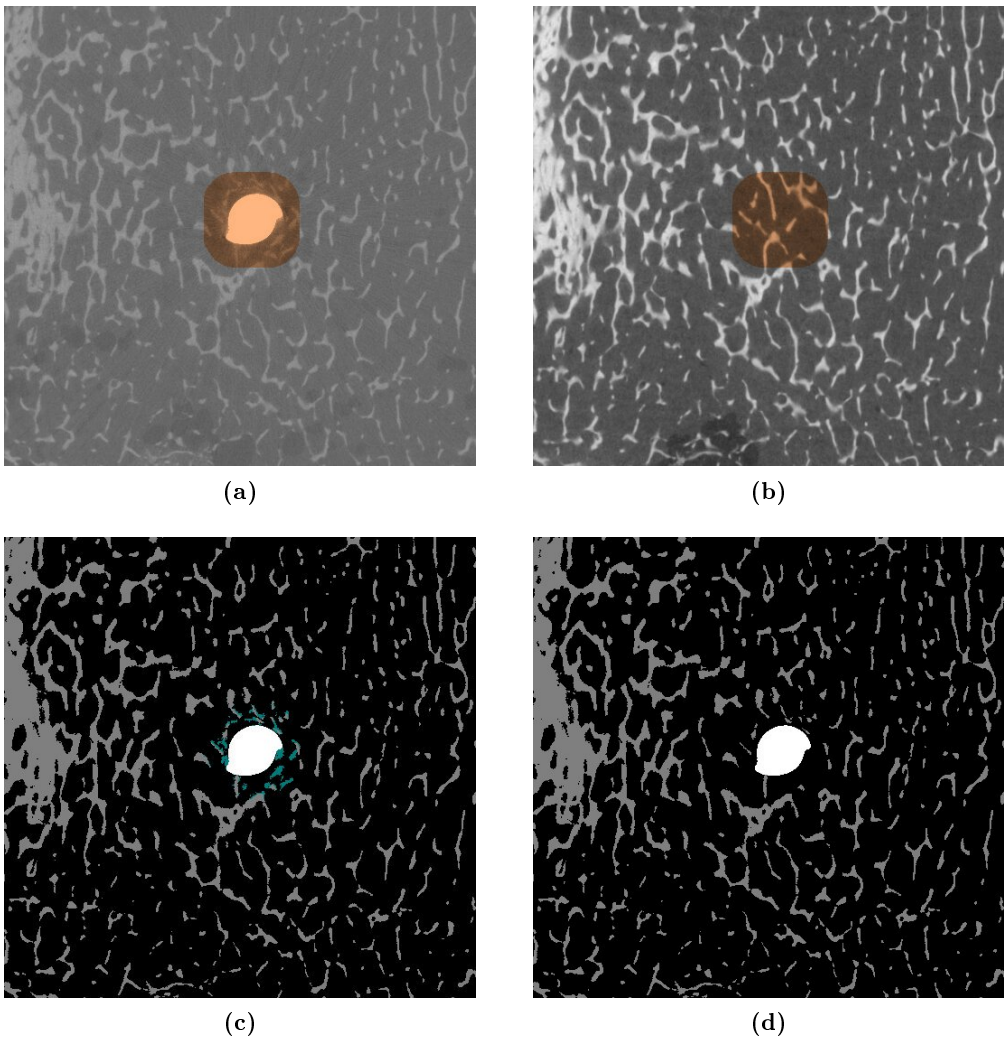

Figure 2.21.: The creation of the model without broken trabeculae. The area that was compared is marked in orange in the CT image of *realScrew* (a) and the CT image of *noScrew* (b). The voxels that were removed are marked in cyan in the segmented image (c). The model after removal of the broken trabeculae is shown in (d).

2.2.5. Meshing

The generation of the finite element mesh was performed with a script available in Medtool that converts each voxel into a linear hexaeder element. Assuming isotropic material each element is assigned material properties (Young's Modulus E, Poisson's ratio ν) corresponding

to its gray scale value (see Table 2.2). As no material test was performed for the bone samples used in this test, the material properties were estimated from the literature. An elastic modulus of $E_{tissue} = 10\ GPa$ was taken from [8], where osteoporotic bone was studied with microindentation. It was assumed that cortical and trabecular bone have the same isotropic material properties. The elastic modulus of titanium was taken from [32]. Models with voxel lengths of 36 μm, 54 μm and 72 μm were created from the original 18 μm CT data to study the influence of mesh resolution.
Table 2.3 gives an overview of all the models that were generated. It shows the number of elements created for each model and the corresponding degrees of freedom (DoFs). The column "restrained nodes" gives the number of nodes on the boundary of the model that were set to zero displacement. The amount of nodes on the screw head onto which the displacement was applied is listed in the table as "fixed nodes".

Material	Gray value	Young's Modulus [GPa]	Poisson's ratio [-]
Bone	1	10	0.3
Titanium	2	105	0.3

Table 2.2.: Material properties used in the FE analysis

	Model	Elements	DoFs	restrained nodes	fixed nodes
realScrew	36 μm	19.6816 Mio.	85.5535 Mio.	169673	123
	36 μm_noT	19.6767 Mio.	85.5505 Mio.	169673	123
	36 μm_noBT	19.3529 Mio.	84.1321 Mio.	169673	123
	54 μm	5.98838 Mio.	29.2238 Mio.	83734	84
	54 μm_noT	5.98535 Mio.	29.2192 Mio.	83734	84
	54 μm_noBT	5.91451 Mio.	28.8925 Mio.	83734	84
	72 μm	2.62319 Mio.	13.9879 Mio.	51595	63
	72 μm_noT	2.62125 Mio.	13.985 Mio.	51595	63
	72 μm_noBT	2.57839 Mio.	13.794 Mio.	51595	63
virtScrew	36 μm	19.6036 Mio.	83.1603 Mio.	166257	123
	36 μm_noT	19.5989 Mio.	83.159 Mio.	166257	123
	54 μm	6.55063 Mio.	30.3536 Mio.	87853	84
	54 μm_noT	6.54699 Mio.	30.3516 Mio.	87853	84
	72 μm	2.60565 Mio.	13.7471 Mio.	49787	63
	72 μm_noT	2.60372 Mio.	13.7457 Mio.	49787	63

Table 2.3.: Details about the meshes generated from the *realScrew* and *noScrew* data.

2.2.6. Boundary Conditions

Neglecting the influence of the embedding the surface nodes at all four cut faces (distal, proximal, medial and lateral) were fixed under the assumption that the stresses would be concentrated around the screw and would not be influenced by the boundary conditions (*St. Venant's Principle*). When the mechanical test is started and the screw is displaced, the rod

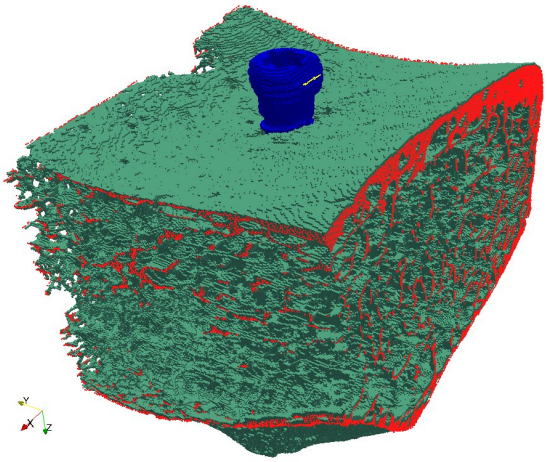

Figure 2.22.: Boundary conditions applied to the model. The fixed nodes are marked in red. The nodes onto which the displacement was applied are marked in yellow.

will not stay in contact with the whole flat surface on the screw head. The contact area will reduce to a contact line. The displacement of the screw was therefore applied on nodes along a line at the border of the flat surface (see Figure 2.23). For comparability reasons it was made sure that the line was at the same coordinates and had the same length for models with different voxel sizes. The nodes were manually selected for each model using the visualization application ParaView (Kitware Inc., USA). Corresponding with the experimental setup the

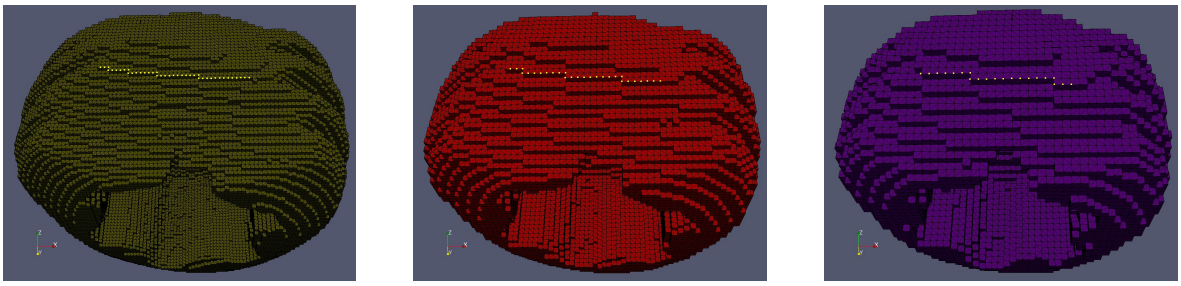

(a) **(b)** **(c)**

Figure 2.23.: The screw head at different resolutions. The nodes onto which the displacement was applied are marked in yellow. The voxel sizes are (a) 36 μm, (b) 54 μm and (c) 72 μm

direction of the displacement was chosen normal to the flat surface. It was assumed that the direction of displacement would not change significantly during the elastic deformation of the bone. By measuring the inclination of the flat surface from the CT image a vectorial displacement

$$\boldsymbol{u} = u \begin{pmatrix} 0.047 \\ 0.86648 \\ 0.497 \end{pmatrix}$$

was derived, where u represents the vertical displacement of the steel rod from the mechanical test. This displacement was applied to each selected node on the screw head.

2.2.7. Solving and Post-Processing

The models were analysed with the linear finite element solver parFE [33]. It is designed to solve large models by parallel computation. parFE uses the *conjugate gradient method* together with a *multigrid preconditioner* to iteratively solve the system of linear equations given by

$$\boldsymbol{K}\boldsymbol{u} = \boldsymbol{f}$$

where $\boldsymbol{K}$ is the global stiffness matrix, $\boldsymbol{u}$ the vector of nodal displacements and $\boldsymbol{f}$ the vector of nodal forces.
The post-processing and visualization of the results was done with ParaView.

3. Results

3.1. Mechanical Test

This section presents the results obtained during the mechanical test of Sample3, taken from the left distal radius of a 93 year old woman. It describes the reaction of the sample to the applied loading in the form of the collected force and displacement data.

The vertical lowering of the steel rod was transmitted to the screw via the flat contact surface on the screw head. This produced a translational and rotational displacement of the screw. As the bone is 10 times less stiff than the screw, the bone was deformed under the loading. At the end of the test the applied load had exceeded the elastic limit of the bone and a permanent plastic deformation remained after removal of the steel rod (Figure 3.1).
The vertical displacement applied to the screw head via the rod and the resulting reaction force of Sample3 are shown in Figure 3.2. At the beginning of the curve a short approximately linear region can be identified up to a force of -50 N. Then a change of slope is noticeable followed by a longer approximately linear region till -150 N. There another change in slope can be seen with a nonlinear continuation until a plateau is reached at -175 N. This region of constant force continues to a displacement of -0.6 mm. From there the force grows again nonlinearly until the maximum compression force of -185.53 N is reached at a displacement of -0.813 mm.
Because of the linear nature of the finite element analysis only the initial (approximately) linear force-displacement relation is of interest for the subsequent FE analysis.

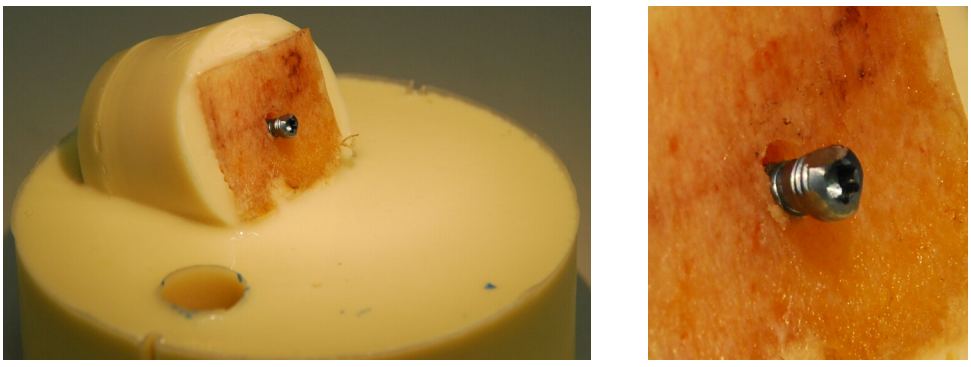

(a) **(b)**

Figure 3.1.: The whole Sample3 after the mechanical test (a) and a detail of the displaced screw head and the deformed cortex (b).

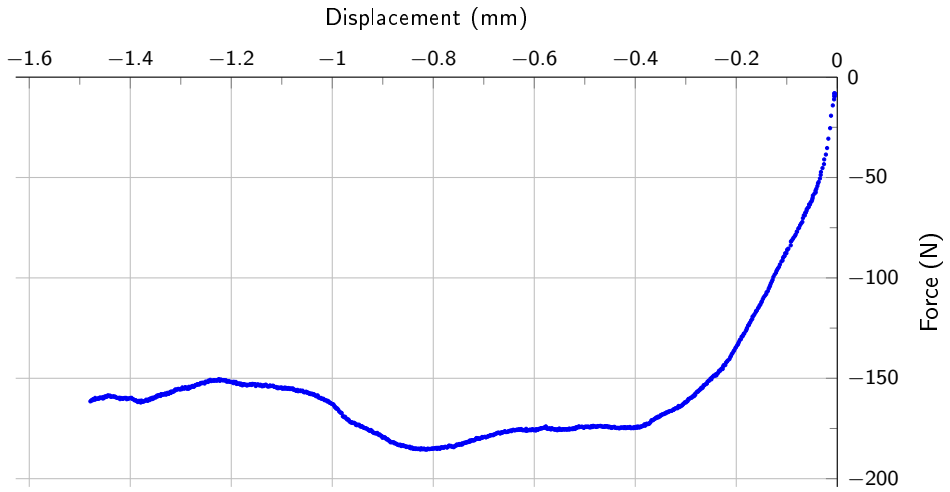

Figure 3.2.: The force-displacement curve of Sample3.

3.2. Finite Element Analysis

In this section the results of the FE analysis are presented and compared to the data from the mechanical test.

3.2.1. Computation Time

The generated FE meshes were solved on a machine with 16 Intel Xeon 3.20 GHz CPUs with 8 GB memory each. Table 3.1 shows the computation time in relation to the voxel lengths used. The non-linear increase in calculation time can be explained with the insufficient amount of memory that was available for the analyses.

Resolution	DoFs	Computation Time
36 μm	85 Mio.	7000 s
54 μm	29 Mio.	1500 s
72 μm	14 Mio.	700 s

Table 3.1.: Computation times for the parFE calculations of models of different resolutions.

3.2.2. Force

Figure 3.3 shows the compression force resulting from an applied screw displacement of 0.025 mm to the 5 different models each calculated for 3 different voxel sizes (36 μm, 54 μm and 72 μm). Two different comparisons can be made. One that looks at influence of the voxel size on the resulting force and another that looks at the influence of the different model configurations.
Comparing the different voxel sizes shows that for each of the 5 models the 72 μm versions generated the highest force values. The results for the 54 μm and 36 μm models are clearly smaller than the 72 μm results and lie close to each other.

The biggest force difference between the 54 μm and the 36 μm mesh can be seen for the *virtScrew* model without tension with 1.07 N (1.47 %), the smallest for the *realScrew* model with −0.23 N (−0.31 %). Comparing the 72 μm models to the 36 μm models gives the biggest difference for the *realScrew* model with −6.75 N (−9.86 %), the smallest for the *virtScrew* without tension with −2.77 N (−3.79 %).
As these results show that the 54 μm results are reasonably close to the ones for the 36 μm models, only the 54 μm results are presented in the following sections.

The different model configurations can be compared with regard to 3 differences:

- Perfect bonding (*realScrew*) $\Longleftrightarrow$ No Tension (*realScrew_noT*):
  16.7 % lower reaction force, when no tension is transferred at the bone/screw interface
- No Tension (*realScrew_noT*) $\Longleftrightarrow$ No Broken Trabeculae (*realScrew_noBT*):
  26.97 % lower reaction force, when the broken trabeculae are removed from the model
- Virtually implanted screw without broken trabeculae (*virtScrew_noT*) $\Longleftrightarrow$ Real Screw without broken trabeculae (*realScrew_noBT*):
  59.95 % higher compression force, when the screw is inserted virtually

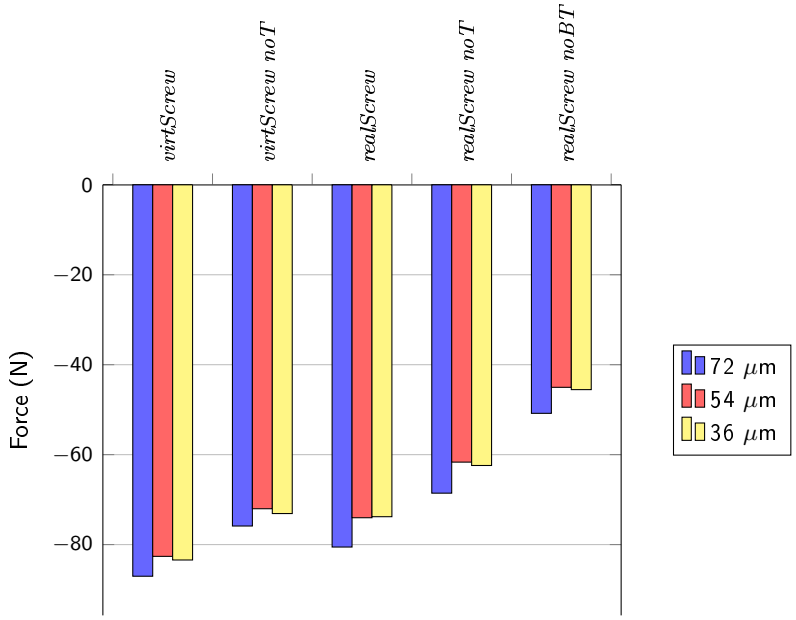

Figure 3.3.: Comparison between the resulting force for realScrew and virtScrew models with different voxel sizes. The applied displacement is 0.025 mm.

3.2.3. Stress

The loading that is applied to the sample leads to stress in the screw and in the bone. Figure 3.4 shows the normal stress in a slice through the 54 μm model of *realScrew* for a deformation of 0.02 mm. The slice lies in the plane defined by the vector of the applied displacement and the axis of the screw. Normal stress in x-direction appears mainly as alternating tension and

compression at the tips and notches of the screw thread. The bone is nearly unaffected by the stress in this direction. Extended zones of elevated normal stress in y-direction can be seen in the peri-implant region near the volar cortex. The region that lies distally from the screw is affected by compression stress, while the region on the proximal side is under tension. Normal stress in z-direction appears mostly in the screw where the distal side is under compression while the proximal side is loaded tensionally. This is the result of the bending moment around the x-axis introduced by the applied displacement.
The normal stress for the 54 μm model of *realScrew_noT* is shown in (Figure 3.5). The displacement is again 0.02 mm and the slice is the same as before. The image of the normal stress in y-direction (3.4b) shows a region of compression in the bone on the distal side of the screw. On the proximal side however there is no tensional stress noticeable which is due to the removal of interface voxels there. The normal stresses in x- as well as z-direction show only marginal differences when compared to the ones in *realScrew*.
Looking at the normal stress in *realScrew_noBT* (Figure 3.6) shows no significant changes for all three components when compared to the *noT* model.

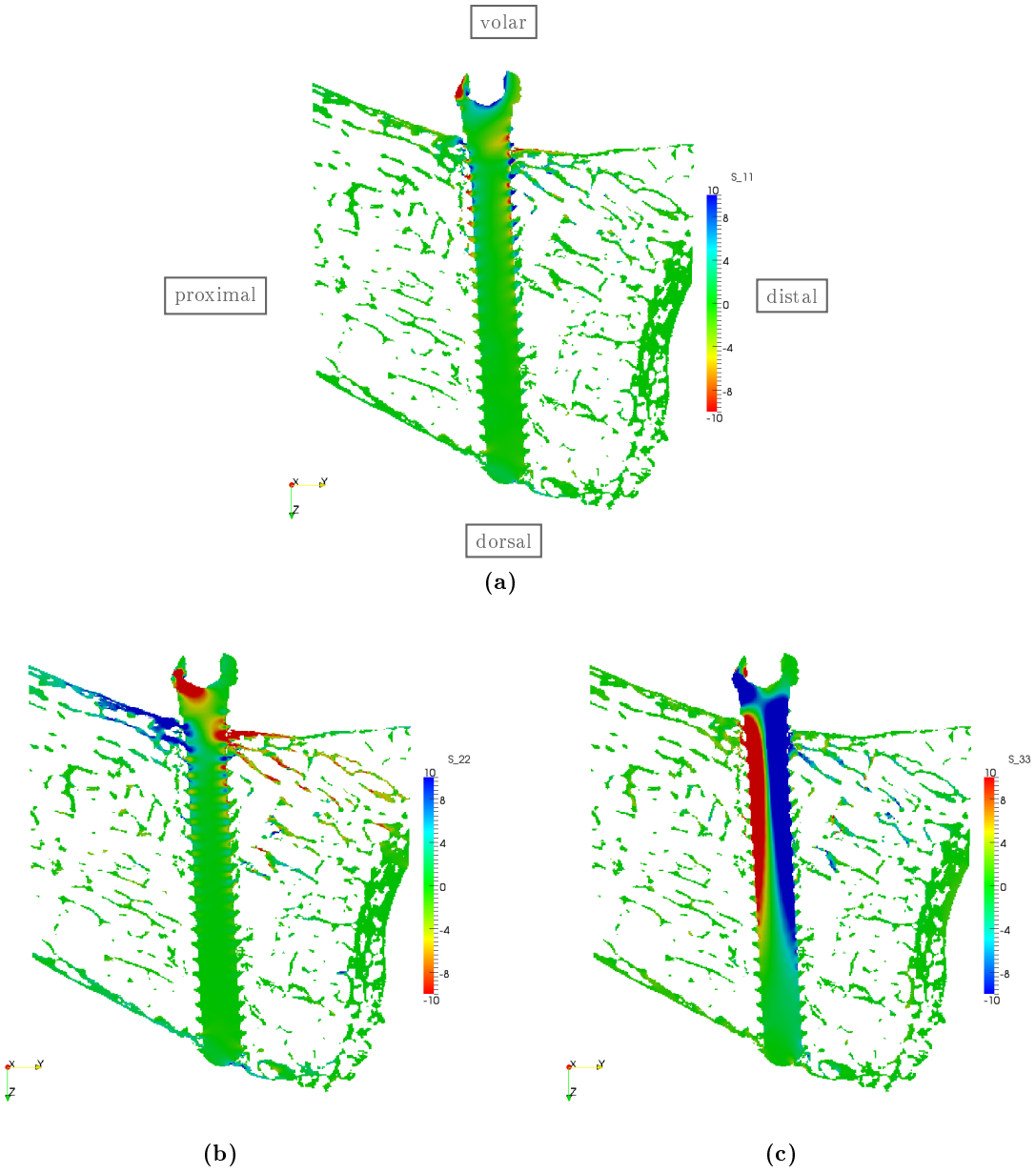

(a)

(b)

(c)

Figure 3.4.: The normal stress in the 54 μm model of *realScrew* in the x-direction (a), the y-direction (b) and the z-direction (c). A displacement of 0.02 mm was applied perpendicularly to the flat surface on the screw head. The anatomical direction used in the text are described in (a).

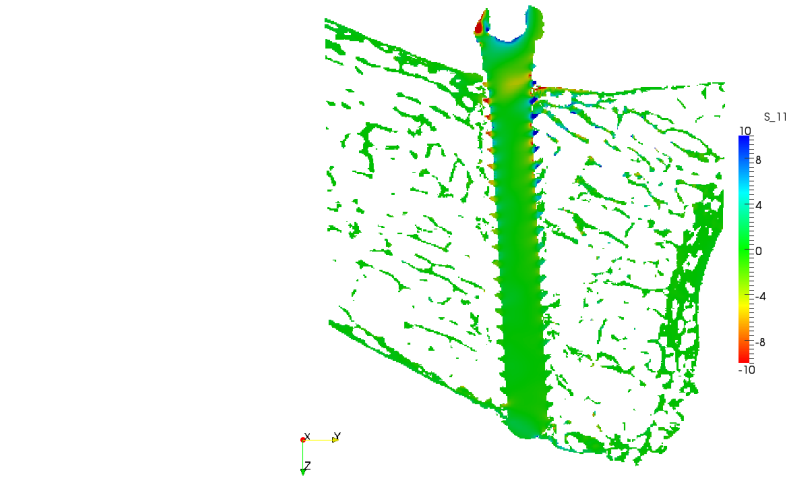

(a)

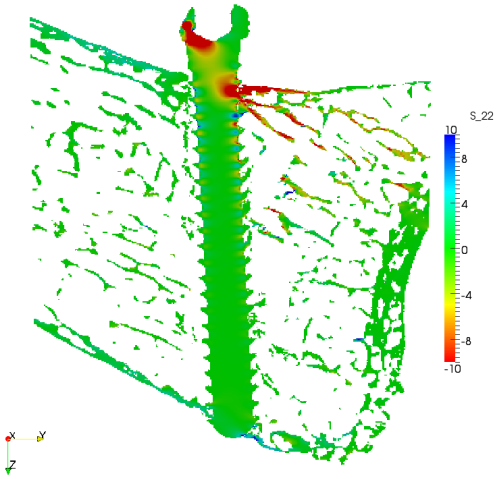

(b)

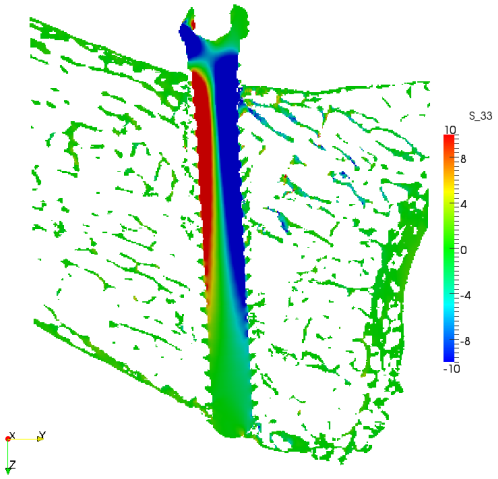

(c)

Figure 3.5.: The normal stress in the 54 μm model of *realScrew_noT* in the x-direction (a), the y-direction (b) and the z-direction (c). A displacement of 0.02 mm was applied perpendicularly to the flat surface on the screw head.

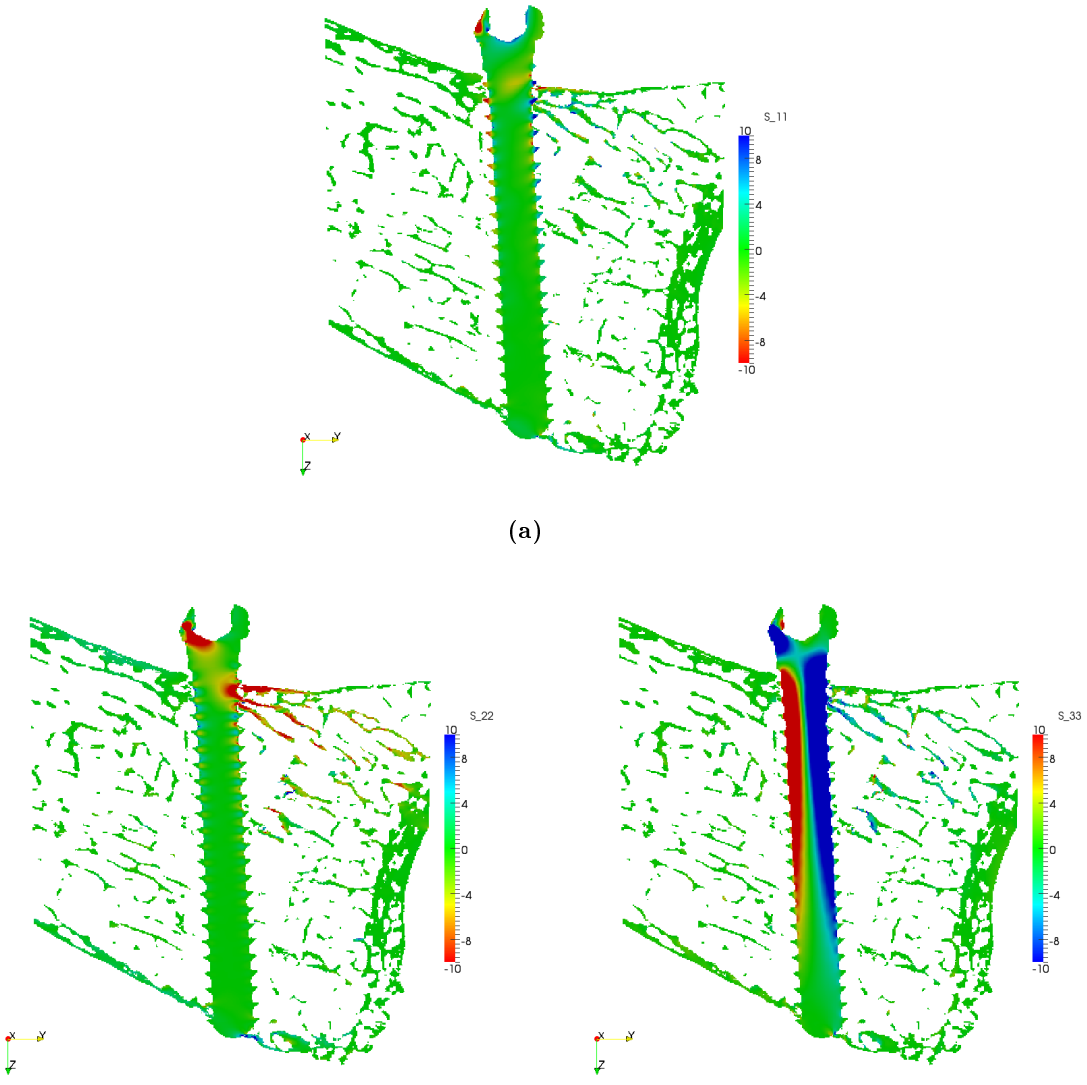

(a)

(b)

(c)

Figure 3.6.: The normal stress in the 54 μm model of *realScrew_noBT* in the x-direction (a), the y-direction (b) and the z-direction (c). A displacement of 0.02 mm was applied perpendicularly to the flat surface on the screw head.

3.2.4. Strain Energy Density

The strain energy density (SED) was used to estimate the onset of yielding in the sample. Under the assumption of bone as a linear elastic material

$$SED = \frac{1}{2}\sigma_{ij}\varepsilon_{ij}$$

where σ_{ij} is the stress tensor and ε_{ij} is the strain tensor [34]. For the purpose of a rough estimation the general stress state in the sample is simplified to a uni-axial stress σ. Together with Hooke's Law this gives the formulation

$$SED = \frac{1}{2}\sigma\varepsilon = \frac{1}{2}E\varepsilon^2$$

where E is the elastic modulus. With this simplified relation a critical strain energy density SED_{crit} for yielding of the bone can be calculated. The tensile yield strain for human vertebrae from [36] (ε_y=0.71%-0.88%) was taken as a reference value. With $E = 10GPa$, this gives a range for the critical strain energy density of 0.25 to 0.39.

The onset of yielding in the mechanical test of Sample3 can be estimated from the measured force-displacement curve. Comparing the curve with a linear regression shows that yielding begins at a rod displacement of $d_y \approx -0.02\ mm$ (Figure 3.7).

This yield displacement was then applied to the 54 μm model of *realScrew_noBT*. Figure 3.8a and Figure 3.8b show a detail of the screw head and the surrounding bone. The SED results are scaled to the upper and lower boundary of SED_{crit}, respectively. For a better overview only those bone elements with $SED > 0.1$ are displayed, all other elements are rendered transparent. Red elements indicate a strain energy density higher than SED_{crit}. The critical elements are all concentrated at the bone/screw interface. The small number of yielding elements and their scattered distribution suggest that 0.02 mm can be used as an estimation for the applied displacement where the sample starts to yield.

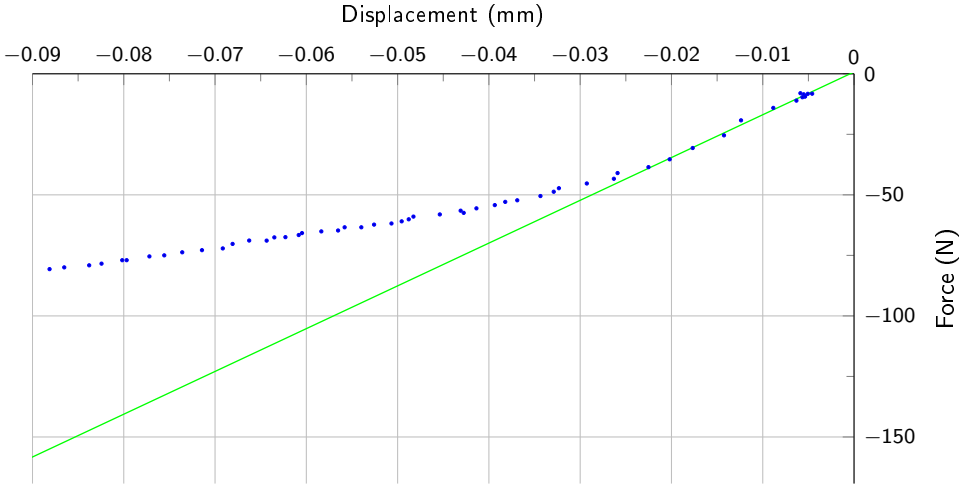

Figure 3.7.: A detail of the measured force-displacement curve of Sample3 and an approximation of the range of elastic deformation (green line).

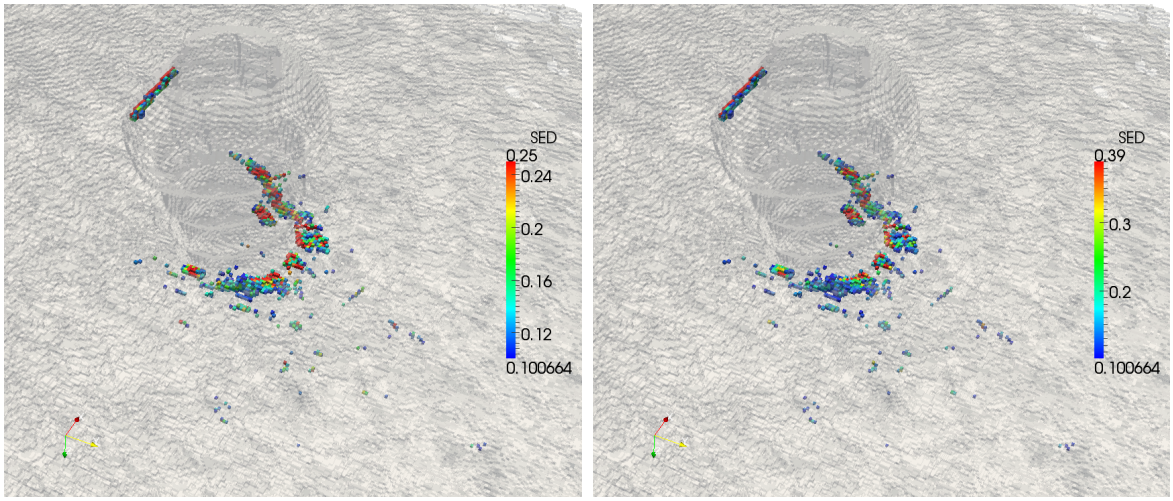

(a) **(b)**

Figure 3.8.: All bone elements with $SED > 0.1$ in the 54 μm model of *realScrew_noBT* for a displacement of 0.02 mm perpendicular to the flat surface on the screw head. The maximum of the scales represents the lower (a) and upper bound of SED_{crit}(b).

3.2.5. Stiffness

For all FE models a spring stiffness value c was derived by dividing the reaction force f by the applied displacement u, which corresponds to the slope of the force-displacement curve. For the mechanical test the stiffness was approximated with a linear regression of the first 13 data points in the force-diplacement plot. Figures 3.9 and 3.10 show the stiffness results for the *realScrew* and the *virtScrew* models. The calculated stiffnesses of all FE models are higher than the stiffness derived from the mechanical test. Those calculated for the *virtScrew* models exceed those of the *realScrew* models. The stiffness of the models decreases with the removal of the tension voxels and even further with the removal of the broken trabeculae. The *realScrew* model overestimates the stiffness of the sample by 67 % (+1185.13 N/mm). For *realScrew_noT* the stiffness is 41 % higher (+729.6 N/mm) than the value calculated from the mechanical test. The *realScrew_noBT* model gives a difference of 3 % (+54.83 N/mm). Looking at the models with the virtually inserted screw gives an overestimation of 89 % (+1570.11 N/mm) for *virtScrew* and 65 % (+1157.07 N/mm) for *virtScrew_noT*.

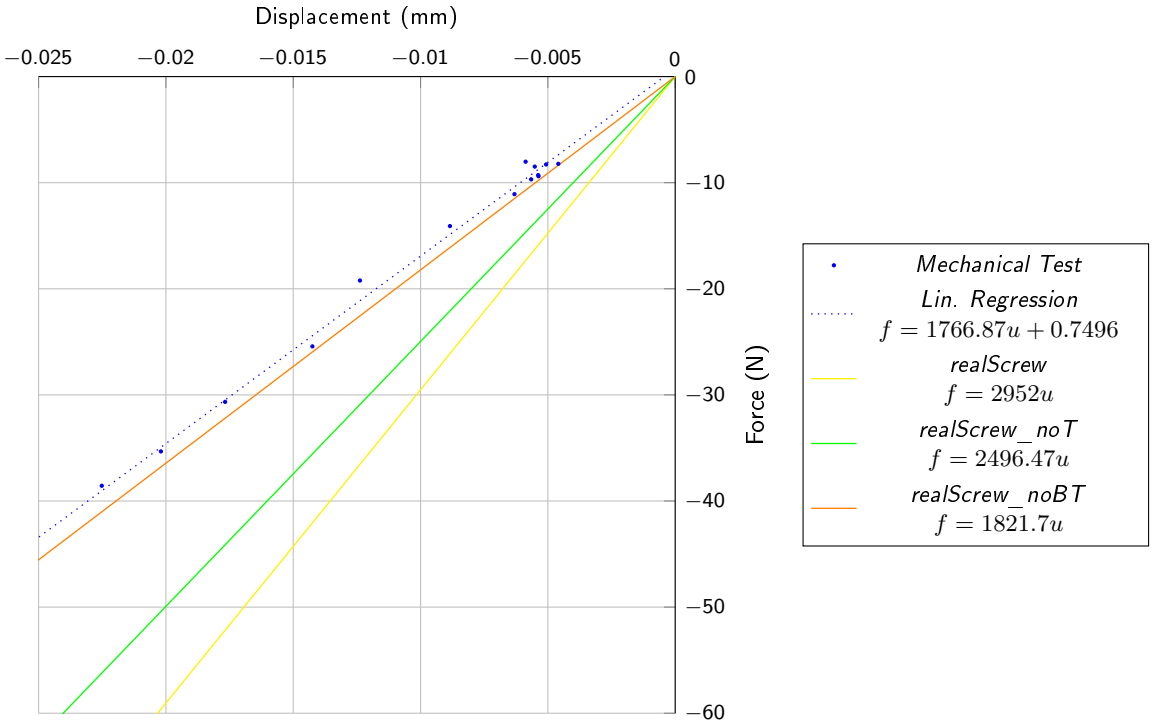

Figure 3.9.: Force-displacement curves of *realScrew* models in comparison with a linear regression of the mechanical test data.

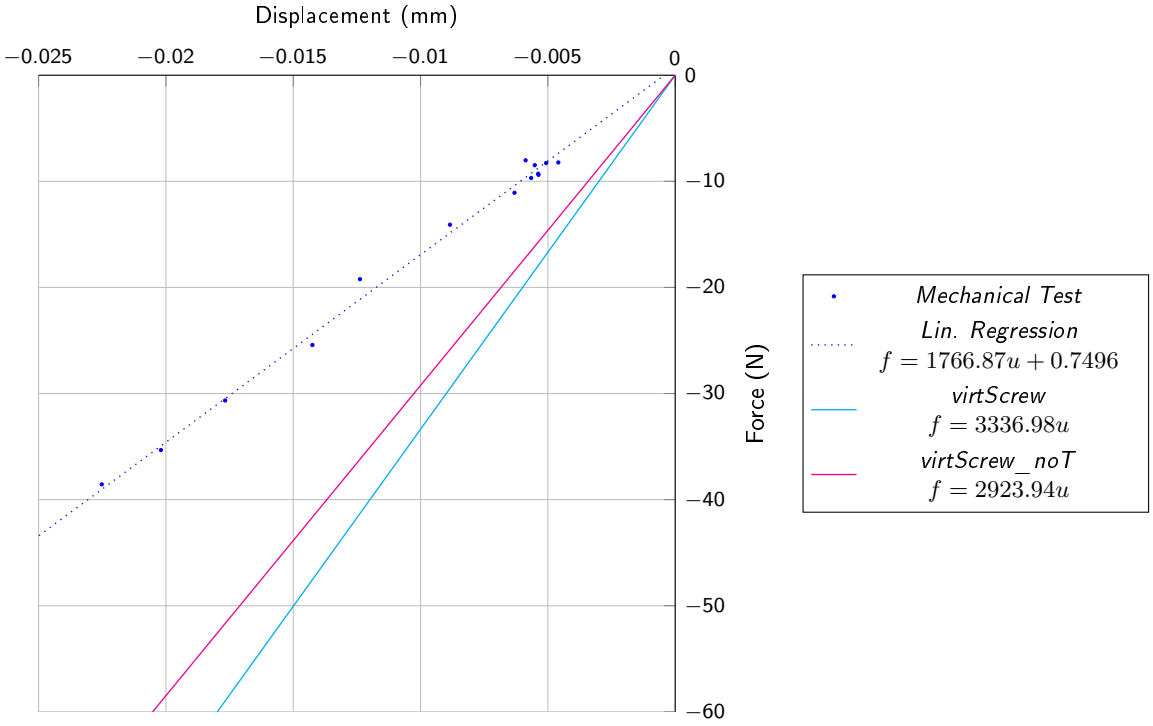

Figure 3.10.: Force-displacement curves of *virtScrew* models in comparison with a linear regression of the mechanical test data.

4. Discussion

Using a mechanical test and a finite element analysis, a simple bone-screw model derived from the volar plate-osteosynthesis of the distal radius can be validated. This chapter discusses the findings of these investigations in light of the limitations found in the study design and its execution. Additionally, possible improvements of the methods used in this thesis are listed.

4.1. Mechanical Test

The mechanical test was performed to obtain experimental data describing the force response of a titanium screw inserted in radius bone and subjected to a defined displacement. These results were used as a reference for a linear FE analysis. Several issues concerning the design, execution and outcome of the mechanical test have to be addressed.

The test design is improvable in different areas. The sample could be rinsed after drilling to remove broken trabeculae, although the majority of the broken trabeculae are probably produced by the implantation of the screw. Furthermore, it has to be noted that in the clinical application the broken trabeculae are beneficial for the in-growth of the screw in the bone.

Further investigations of the exothermic hardening process of the embedding material are advisable. One issue is the decrease in volume during this process. The contraction of the material can lead to a displacement of the embedded sample. A vertical displacement, as was observed in this study for Sample3, can be compensated with a repositioning of the MTS steel rod. A horizontal displacement is acceptable as long as the cross section of the rod fully covers the flat area of force application on the screw head. A rotation of the sample on the other hand will lead to a corrupted test because a moment about the screw axis is applied when lowering the rod. This happened for Sample4 and rendered it unusable for further analysis. Another issue is the heat that is generated during the hardening process. While it is unlikely that the resulting temperature is high enough to change the material properties of the bone, an oily discharge was observed on the sample after the hardening of the embedding that is suspected to be liquefied bone marrow. This could possibly affect the mechanical behaviour of the interface between embedding and bone as well as between screw and bone.

With these issues in mind, the mechanical test of Sample3 was successfully performed following the steps outlined in Section 2.1. No displacement or deformation of the embedding and no detachment between the first and second embedding were noticed during the experiment. The bone was deformed locally in the peri-implant region and the applied displacement exceeded the elastic range of the material. The force-displacement curve was found to show a distinctly non-linear behaviour. A linear relation can only be seen up to a displacement of 0.02 mm.
While in this study only one sample was used to investigated the feasibility of different modelling techniques further research should include bigger sample sizes. For a more detailed investigation of the deformations in the peri-implant region a method like the strain mapping

approach used in [27] could be of interest.

4.2. Finite Element Analysis

Working FE models could be generated from the CT data of *realScrew* as well as *noScrew*. The FE analysis was executed with the focus on the pre-processing aspects. The different steps necessary to generate a finite element model of the bone-screw system were examined. Several limitations concerning the design of the FE analysis have to be addressed:

- **Type of analysis:** The use of linear analysis only accounts for elastic material behaviour, small deformations and perfect bonding between screw and bone. Contact or friction were not investigated. Although this has a considerable effect in the non-linear regime, the predictions at small strains should be reliable.
- **Embedding:** The embedding was not included in the finished models but was represented by fixing the 4 cropped sides of the sample and leaving the dorsal cortex unrestrained. This overestimates the stiffness at the cropped sides and underestimates the fixation at the dorsal cortex. This will have an influence on the global deformations but will have negligible effect on the predicted stresses.
- **Loading:** The area that is affected by the loading with the steel rod changes during the test from an initial surface load to a linear distributed load due to the tilting of the screw. In the FE model a constant displacement distributed along a line is used. This should, however, be negligible as long as small overall displacements are considered.
- **Material Properties:** No material tests were performed on the radius sample. The elastic modulus and the Poisson's ratio were therefore estimated from values reported in the literature. Furthermore, it was assumed that cortical and trabecular bone have the same material properties. Nevertheless tissue material properties were taken from a rigorous study [7] and should be close to the real values.

The CT scans of the bone sample with and without screw lead to the desired images of the sample. However, the 18 μm model had to be scaled down to 36, 54 and 72 μm for computational reasons. A precise alignment of the screw in the CT sample holder could lead to improvements in terms of metal artifacts. According to [26] centering the screw axis in the CT sample holder is beneficial to the reduction of metal artifacts in the scan, but this strategy could not be applied in this study.

The registration procedure provided sufficient alignment of the *realScrew* and the *noScrew* images. Nevertheless, two possibilities to improve this step were found. Using a bigger region (or the whole sample) in the iteration could improve the accuracy of the alignment. Making sure that the sample with and without the screw are oriented as similarly as possible during the scanning process could provide a better starting point for the subsequent registration. To eliminate the need for registration completely, the sample would have to be embedded and implanted directly in a custom made sample holder. This would ensure that the CT scans with and without the screw are already properly aligned.

The algorithm applied to the *realScrew* image in order to reduce the metal artifacts produced satisfying results. The bright ring around the screw could be successfully removed

with little distortion of the bone structure in the peri-implant region. More advanced methods of metal artifact reduction like the ones described in [37] could further improve the results.

The fact that the different materials have overlapping ranges of voxel values made a compromise in the segmentation process necessary as no distinct threshold could be derived from the histograms. It had to be selected by trial and error from visual comparison between CT and segmented data. This is, however, a general challenge found in biomechanical investigations and not limited to this thesis.

The comparison of meshes with different element sizes suggests, that the 54 μm model is sufficent for the calculations executed in the course of this thesis. This model has the advantage of being computationally less costly while giving the same force response as the 36 μm model. The 72 μm model showed errors of up to 9.86 %. It could be argued that a voxel length of 72 μm is already close to the thickness of individual trabeculae in certain areas of the model and therefore not sufficent to resolve the osteoporotically deteriorated microarchitecture of Sample3.
The results from the comparison of *realScrew* with *realScrew_noT* suggest that detailed modelling of the bone-screw interaction is important. Allowing the transmission of tension across the interface leads to a 67 % over-estimation of the stiffness of the model. One way to get more information about the interface would be a contact definition at the interface nodes. This necessitates a non-linear FE model, which is computationally very costly for the amount of degrees of freedom generated in this study. Currently there is no package for parallel non-linear FE calculation available on the market.
A possible way forward could be a submodel approach. First the whole sample is calculated with a coarse mesh. Then the displacements from that mesh are mapped to a model that contains only the screw and the peri-implant region, but has a finer mesh and a contact definition at the interface nodes.

The drilling of the pilot hole and the insertion of the self-tapping screw were found to be highly influential in the generation and computation of the FE models as the procedure causes individual trabeculae to break and dislocate. First, the broken trabeculae had to be identified in the model generation process to distinguish them from the intact trabeculae. The method applied in this study is based on the comparison of the *realScrew* data with the *noScrew* data. The reliability of this approach is dependent on the accuracy of the registration. Second, the breaking and dislocation of trabeculae weakens the bone in the peri-implant region. This is suspected to be partly responsible for the stiffness difference between the *realScrew* and the *virtScrew* models as documented in Section 3.2.5.

Comparing the *realScrew* with the *virtScrew* model suggests that for the model used in this thesis simply inserting the screw virtually into the bone does not give satisfying results. The virtual approach overestimates the stiffness of the sample by 89 %, because it does not take into account the distortion of the trabecular structure caused by the implantation procedure of the screw.
One additional issue that surfaced when comparing the realScrew with the virtScrew model is the difference in trabecular structure that is not apparent in the cropped cuboid used in the segmentation process. The virtScrew model has thicker trabeculae and higher trabecular connectivity. These differences could stem from the CT scanning process where the presence

of the titanium screw has an image distorting influence far away from the screw. A second possibility is that the differences are introduced by the registration process, where the interpolation associated with the rotation and translation applied during the procedure cause trabeculae to become thicker and more connected.

The over-estimation of the stiffness of the bone sample which was found for all models of *realScrew* and *virtScrew* is in accordance with the results found in [26]. In that paper a pull-out test on a titanium screw in a sheep vertebra was investigated with mechanical test and FE simulation. There the stiffness calculated from the model was found to be 9 times higher than the measured data. Bearing in mind the different loading scenario (tension in [26] and shear-bending in this thesis) the modeling approach taken in this thesis resulted in a minimum stiffness over-estimation of 3 % for *realScrew_noBT*.

Taking into account the limitations mentioned above, comparing the results of the mechanical test and the FE analysis leads to the conclusion that a detailed modeling of the peri-implant region is necessary to describe the mechanical behaviour of screw and bone. The way both the interface of bone and screw as well as the broken trabeculae are handled has a huge influence on the results of the analysis. Virtually inserting the screw into the image produced a severe over-estimation of the stiffness of the sample.

A. Metal Artifact Reduction Script

The following MATLAB script was adopted from an existing code developed by Lukas Fischer and René Donner at the CIR lab at the AKH Wien.

```
function artiRed(filename, nBorder)
% artiRed(filename, nBorder) reads filename.mhd and filename.raw,
% applies a filter to reduce metal artifacts inside a radius given
% by nBorder and stores the filtered data in the new files
% filenameFiltered.mhd and filenameFiltered.raw.
% Input filename without file extension.
%
% Example:
% To filter data from a test.mhd and test.raw with a radius of 30
% Input: artiRed('test', 30)
% Output: testFiltered.mhd and testFiltered.raw

% Add file extensions
mhdInFilename = strcat(filename, '.mhd');
mhdOutFilename = strcat(filename, 'Filtered.mhd');
rawInFilename = strcat(filename, '.raw');
rawOutFilename = strcat(filename, 'Filtered.raw');

% Open the .mhd-file and read the size of the raw data into a cell
mhdIn = fopen(mhdInFilename,'r');
mhdInContent = fscanf(mhdIn,'%c',inf);
fclose(mhdIn);
rawDims = regexp(mhdInContent, 'DimSize = (\d+)\s(\d+)\s(\d+)', 'tokens')
rawDimX = str2double(rawDims{1}(1))
rawDimY = str2double(rawDims{1}(2))
rawDimZ = str2double(rawDims{1}(3))

% Open the .raw-file and read the data slice by slice
rawIn = fopen(rawInFilename,'r','n');
rawOut = fopen(rawOutFilename,'w','n');
for k = 1:rawDimZ
    slice = fread(rawIn,[rawDimX,rawDimY],'uint8');
    name = strcat('testSlice',num2str(k),'.gif');
    slice = uint8(slice);

    % Apply filter
    if k <= 382
        % Mask the bone. Turn all pixels black except for the
        % ones with the highest values (=screw)
        mask = slice == max(slice(:));

        % For every pixel in the image calculate the distance to
        % the nearest screw pixel
        dists = bwdist(mask);
```

```
45
46          % Calculate the mean of equidistant pixels
47          for x = 1:2*nBorder
48              indices{x} = dists>x/2-0.5 & dists<=x/2;
49              means(x) = mean(slice(indices{x}));
50          end
51
52          % Calculate baseline from the outermost mean values and
53          % plot means and baseline
54          baseline = mean(means(end-10:end));
55
56          if k == uint16(rawDimZ/2)
57              plot(means); hold on; plot(1:numel(means),baseline,'r');
58              title('mean pixelvalue of equidistant pixels around screw');
59              xlabel('distance from screw');
60              ylabel('mean pixel value');
61          end
62          differences = means-baseline;
63
64          % For equidistant pixels subtract the difference
65          sliceFiltered = slice;
66          for x = 1:2*nBorder
67              sliceFiltered(indices{x}) = sliceFiltered(indices{x})-
                    differences(x);
68          end
69      else
70          sliceFiltered = slice;
71      end
72
73      sliceFiltered = uint8(sliceFiltered);
74      name = strcat('testSliceF',num2str(k),'.gif');
75
76      % Write filtered slices to new .raw-file
77      fwrite(rawOut, sliceFiltered,'uint8');
78  end
79  fclose(rawIn);
80
81  % Write new .mhd-file
82  mhdOutContent = strrep(mhdInContent, rawInFilename, rawOutFilename);
83  mhdOut = fopen(mhdOutFilename,'w','n');
84  fwrite(mhdOut, mhdOutContent);
85  fclose(mhdOut);
86  end
```

Bibliography

[1] Webster S. S. Jee. *Bone Mechanics Handbook*, chapter Integrated Bone Tissue Physiology: Anatomy and Physiology, pages 1–1–1–68. CRC Press LLC, 2001.

[2] Stephen Weiner and Wolfie Traub. Bone structure: from angstroms to microns. *FASEB J*, 6:879–885, 1992.

[3] Jae-Young Rho, Liisa Kuhn-Spearing, and Peter Zioupos. Mechanical properties and the hierarchical structure of bone. *Medical Engineering & Physics*, 20:92–102, 1998.

[4] Peter Varga. *Prediction of distal radius fracture load using HR-pQCT-based finite element analysis*. PhD thesis, TU Wien, 2009.

[5] B Lawrence Riggs and A Michael Parfitt. Drugs used to treat osteoporosis: The critical need for a uniform nomenclature based on their action on bone remodeling. *Journal of Bone and Mineral Research*, 20(2):177–184, 2005.

[6] Harold M Frost. A 2003 Update of Bone Physiology and Wolff's Law for Clinicians. *Angle Orthodontist*, 74(1):3–15, 2004.

[7] Uwe Wolfram, Hans-Joachim Wilke, and Philippe K. Zysset. Valid μ finite element models of vertebral trabecular bone can be obtained using tissue properties measured with nanoindentation under wet conditions. *Journal of Biomechanics*, 43(9):1731–1737, 2010.

[8] A M Coats, P Zioupos, and R M Aspden. Material properties of subchondral bone from patients with osteoporosis or osteoarthritis by microindentation testing and electron probe microanalysis. *Calcified Tissue International*, 73:66–71, 2003.

[9] C. E. Hoffler, K. E. Moore, K. Kozloff, P. K. Zysset, M. B. Brown, and S. A. Goldstein. Heterogeneity of bone lamellar-level elastic moduli. *Bone*, 26(6):603–609, Jun 2000.

[10] X Edward Guo. *Bone Mechanics Handbook*, chapter Mechanical Properties of Cortical Bone and Cancellous Bone Tissue, pages 10–1–10–23. CRC Press LLC, 2001.

[11] WHO. Assessment of fracture risk and its application to screening for postmenopausal osteoporosis. Technical report, WHO, 1994.

[12] Lawrence G. Raisz. Pathogenesis of osteoporosis: concepts, conflicts, and prospects. *The Journal of Clinical Investigation*, 115(12):3318–3325, 2005.

[13] Bernhard N. Tilmann. *Atlas der Anatomie des Menschen*. Springer Berlin / Heidelberg, 2005.

[14] Jane A. Barrett, John A. Baron, Margaret R. Karagas, and Michael L. Beach. Fracture Risk in the U.S. Medicare Population. *Journal of Clinical Epidemiology*, 52(3):243 – 249, 1999.

[15] Soufiane Boufous, Caroline Finch, Stephen Lord, Jacqueline Close, Todd Gothelf, and William Walsh. The epidemiology of hospitalised wrist fractures in older people, New South Wales, Australia. *Bone*, 39(5):1144–1148, 2006.

[16] T. W. O'Neill, C. Cooper, J. D. Finn, M. Lunt, D. Purdie, D. M. Reid, R. Rowe, A. D. Woolf, W. A. Wallace, and U. K. Colles' Fracture Study Group. Incidence of Distal Forearm Fracture in British Men and Women. *Osteoporos Int*, 12(7):555–558, 2001.

[17] Medartis AG, Basel, Switzerland. *APTUS Wrist Distal Radius System 2.5 Surgical Technique*, 2011.

[18] Maria K T Wilcke, Hassan Abbaszadegan, and Per Y Adolphson. Wrist function recovers more rapidly after volar locked plating than after external fixation but the outcomes are similar after 1 year. *Acta Orthopaedica*, 82(1):76–81, 2011.

[19] Corey Trease, Terence McIff, and E. Bruce Toby. Locking Versus Nonlocking T-Plates for Dorsal and Volar Fixation of Dorsally Comminuted Distal Radius Fractures: A Biomechanical Study. *The Journal of Hand Surgery*, 30(4):756–763, 2005.

[20] Denju Osada, Shuzo Kamei, Koichiro Masuzaki, Morimitsu Takai, Masahiro Kameda, and Kazuya Tamai. Prospective Study of Distal Radius Fractures Treated With a Volar Locking Plate System. *The Journal of Hand Surgery*, 33(5):691–700, 2008.

[21] Markus Figl, Patrick Weninger, Josef Jurkowitsch, Marcus Hofbauer, Josef Schauer, and Martin Leixnering. Unstable Distal Radius Fractures in the Elderly Patient–Volar Fixed-Angle Plate Osteosynthesis Prevents Secondary Loss of Reduction. *J Trauma*, 68(4):992–998, Apr 2010.

[22] Matthew D. Putnam, Nicholas J. Meyer, Eric W. Nelson, David Gesensway, and Jack L. Lewis. Distal radial metaphyseal forces in an extrinsic grip model: Implications for postfracture rehabilitation. *The Journal of Hand Surgery*, 25(3):469–475, 2000.

[23] Herwig Drobetz, Adam L. Bryant, Tom Pokorny, Ralf Spitaler, Martin Leixnering, and Jesse B. Jupiter. Volar Fixed-Angle Plating of Distal Radius Extension Fractures: Influence of Plate Position on Secondary Loss of Reduction–A Biomechanic Study in a Cadaveric Model. *The Journal of Hand Surgery*, 31(4):615.e1–615.e9, 2006.

[24] Dieter H. Pahr and Philippe K. Zysset. A comparison of enhanced continuum FE with micro FE models of human vertebral bodies. *Journal of Biomechanics*, 42(4):455–462, 2009.

[25] Peter Varga, Dieter H. Pahr, Sebastian Baumbach, and Philippe K. Zysset. HR-pQCT based FE analysis of the most distal radius section provides an improved prediction of Colles' fracture load in vitro. *Bone*, 47(5):982–988, November 2010.

[26] Andreas Wirth, Thomas Mueller, Wim Vereecken, Cyril Flaig, Peter Arbenz, Ralph Müller, and G. Harry van Lenthe. Mechanical competence of bone-implant systems can accurately be determined by image-based micro-finite element analyses. *Archive of Applied Mechanics*, 80:513–525, 2010.

[27] S. E. Basler, T. L. Mueller, D. Christen, A. J. Wirth, R. Muller, and G. H. van Lenthe. Towards validation of computational analyses of peri-implant displacements by means of experimentally obtained displacement maps. *Comput Methods Biomech Biomed Engin*, 14(2):165–174, Feb 2011.

[28] Medartis AG, Basel, Switzerland. *ADAPTIVE Distal Radius System 2.5*, 2010.

[29] Florian Schacherreiter. Reinforcement of PU as embedding material. Technical report, TU Wien, 2010.

[30] Luis Ibanez, Will Schroeder, Lydia Ng, and Josh Cates. *The ITK Software Guide*. Insight Software Consortium, 2005.

[31] D. Mattes, D. R. Haynor, H. Vesselle, T. K. Lewellen, and W. Eubank. Pet-ct image registration in the chest using free-form deformations. *Medical Imaging, IEEE Transactions on*, 22(1):120–128, 2003.

[32] Alfred Buch. *Pure metals properties: a scientific-technical handbook*. ASM International, Materials Park, Ohio, 1999.

[33] Peter Arbenz, G. Harry van Lenthe, Uche Mennel, Ralph Mueller, and Marzio Sala. A scalable multi-level preconditioner for matrix-free μ-finite element analysis of human bone structures. *International Journal for Numerical Methods in Engineering*, 73(7):927–947, 2008.

[34] C. O. Horgan. On the strain-energy density in linear elasticity. *Journal of Engineering Mathematics*, 7:231–234, 1973.

[35] R. von Mises. Mechanik der festen Körper im plastisch deformablen Zustand. *Göttin. Nachr. Math. Phys.*, 1:582–592, 1913.

[36] David L Kopperdahl and Tony M Keaveny. Yield strain behavior of trabecular bone. *Journal of Biomechanics*, 31(7):601–608, 1998.

[37] Oliver Watzke and Willi A Kalender. A pragmatic approach to metal artifact reduction in CT: merging of metal artifact reduced images. *Eur Radiol*, 14(5):849–856, May 2004.